AIAA JOURNAL
Vol. 53, No. 12, December 2015

Investigation of Fan-Wake/Outlet-Guide-Vane Interaction Broadband Noise

Hongbin Ju,* Ramani Mani,† Martin Vysohlid,‡ and Anupam Sharma§
GE Global Research, Niskayuna, New York 12309

DOI: 10.2514/1.J053167

Fan-wake/outlet-guide-vane interaction broadband noise in turbofan jet engines is studied. The mechanism and some issues are first discussed using a two-dimensional gust-prediction model. An oblique gust-prediction model is then developed. Quasi-three-dimensional unsteady lift is calculated using a two-dimensional equivalence method. It is coupled with annular duct modes to obtain the sound power spectrum density. Spanwise turbulence integral length scales and their impact on power spectrum density predictions are investigated. A spanwise integration limit suitable for the complete frequency range is proposed. The model is validated using the NASA Source Diagnostic Test data. Sound power scaling with vane count B is examined. If solidity is maintained, the cascade response does not converge on the single-airfoil response, even for low vane counts. The sound power varies inversely with B at low frequency; it scales with B at very high frequency. The power spectrum density trend with the fan tip Mach number M_T is also identified. It scales with M_T^5 if turbulence intensity in the fan wake scales "ideally" with M_T. At offdesign conditions, fan wakes are not ideal; therefore, different speed trends apply. $M_T^{3.3}$ scaling is found to best fit the Source Diagnostic Test data and the prediction.

Nomenclature

a_d	=	sound speed of acoustic medium in the exhaust duct
B	=	number of outlet guide vanes
C	=	airfoil chord length
$\hat{h}^{\pm}_{mn}(k_1, k_2, k_3)$	=	chordwise integrated unsteady lift
$\hat{h}^{+}_{s}$	=	$\sqrt{\sum \lvert\hat{h}^{+}_{mn}\rvert^2}$ (summation over all the cut-on modes)
k_d	=	ω/a_d; acoustic wave number for the acoustic medium in the exhaust duct
k_1, k_2, k_3	=	wave numbers in ξ, η, and z directions, respectively
M_d	=	u_d/a_d
M_T	=	fan tip Mach number
m	=	spinning mode number
n	=	radial mode index
R_i, R_o	=	radii of the inner duct and the outer duct
r	=	radial coordinate
S	=	spacing between blades in the linear cascade
u_d	=	mean velocity of acoustic medium in the exhaust duct
u_0	=	mean flow velocity
w	=	time-averaged upwash velocity $\sqrt{(2/3)\text{TKE}}$
$\hat{w}$	=	Fourier component of the upwash velocity
x	=	axial coordinate
y	=	tangential coordinate in the unwrapped cascade
z	=	spanwise coordinate
$\alpha^{\pm}_{mn}$	=	axial wave numbers in the downstream ($+x$) and upstream ($-x$) directions, respectively
β	=	wave number in y direction
Γ_{mn}	=	normalization factor of radial mode eigenfunction
η	=	chord-normal coordinate on the reference blade
θ	=	stagger angle of the linear cascade
κ_{mn}	=	$\sqrt{k_d^2 - (1 - M_d^2)\mu_{mn}^2}$
Λ	=	turbulence integral length scale
λ	=	$\omega C/u_0$; reduced frequency, wavelength
μ_{mn}	=	radial eigenvalue in the annular duct
ξ	=	chordwise coordinate on the reference blade
ρ_d	=	density of acoustic medium in the exhaust duct
ρ_0	=	density of the mean flow
σ	=	interblade phase angle
$\Phi_{ww}(k_1, k_2, k_3)$	=	upwash velocity spatial cross-power spectral density
$\Psi_m(\mu_{mn})$	=	radial eigenfunction of the annular duct
ω	=	circular frequency
ϖ	=	turbulence dissipation rate
$\pm$	=	downstream (+) and upstream (−) propagations

Presented as Paper 2013-2151 at the 19th AIAA/CEAS Aeroacoustics Conference, Berlin, Germany, 27–29 May 2013; received 30 October 2013; revision received 23 April 2015; accepted for publication 21 June 2015; published online 15 October 2015.

*Aerodynamics and Acoustics Laboratory, One Research Circle; juh@ge.com. Senior Member AIAA.

†Aerodynamics and Acoustics Laboratory, One Research Circle. Associate Fellow AIAA.

‡Fluid Mechanics Laboratory, One Research Circle; vysohlid@ge.com. Member AIAA.

§Aerodynamics and Acoustics Laboratory, One Research Circle; currently Iowa State University, Ames, IA 50011. Senior Member AIAA.

I. Introduction

IN TURBOFAN jet engines, the dominant sources of jet noise are quadrupoles, whereas dipoles dominate fan noise. Sound power from a quadrupole scales with the flow Mach number as M^8, and that from a dipole scales with $M^{4\sim6}$. As the bypass ratio (BPR) increases, the jet velocity and (hence) jet noise are significantly reduced; and the fan noise (tone and broadband) becomes important. For the GE90 engine, the fan exhaust (FEX) noise is comparable with jet noise at takeoff; it is higher than jet noise at cutback and approach [1]. This trend continues in modern turbofan engine designs. The FEX noise tends to overtake jet noise and dominates at all conditions. The fan tone noise is significantly reduced at a high BPR, as the pressure ratio and fan tip speed are lower. It is also controllable through mitigation technologies, such as choosing a blade/vane count ratio to cut off the fundamental blade-passing tone, increasing the spacing between airfoil rows, sweeping and leaning vanes, installing acoustic liners, etc. However, even if all fan tones are eliminated, the total system noise will only be reduced by 0.5 to 1.5 effective perceived noise level

in decibels (EPNdB) [2]. On the other hand, reducing fan broadband noise (BBN) can yield a 3 to 4 EPNdB reduction in engine system noise. Over the past 50 years, research focus has been on jet noise and fan tone noise. Interest in research into fan BBN is growing to meet the challenges in modern engine designs. One of the recent developments at the NASA John H. Glenn Research Center is to build a facility to investigate fan BBN.[¶] In Europe, two consecutive projects, PROBAND and FLOCON, are devoted to turbofan broadband noise prediction and reduction [3].

There are two types of fan BBN: 1) "self" noise, which is generated by the scattering of boundary-layer turbulence by airfoil trailing edges (TEs); and 2) interaction noise, which is generated by upstream turbulence impinging on a downstream blade row [4]. Recent experiments suggest that the dominant broadband noise source at all speeds is the interaction of fan-wake turbulence flow with outlet guide vanes (OGVs) [5]. Self-noise is important only at low M_T [6,7]. Fan–inflow turbulence interaction noise is important at high M_T [8].

In this paper, we focus on broadband noise generated by fan-wake–OGV interaction. To develop a prediction tool, three steps are involved: 1) harmonic cascade analysis, 2) broadband modeling, and 3) code development and validation. In the first step, the interaction of a plane vorticity wave (harmonic, both in space and time) with a single airfoil or a cascade is modeled [9]. Some analytical methods have been developed, such as those by Amiet [10] and Adamczyk [11] [three-dimensional (3-D) gust/single airfoil], Envia [12] (3-D gust/annular cascade at high frequency), Glegg [13], Posson et al. [14] (3-D gust/linear cascade), etc. Semianalytical models are also available, such as the lift model by Namba [15] for 3-D gust/annular cascade, the two-dimensional (2-D) lift model by Ventres et al. [16], and the bound vorticity 2-D model LINearized SUBsonic unsteady flow in cascade (LINSUB) by Smith [17].

The flow and geometries are simplified for analytical treatments in these harmonic cascade analyses. How to apply them in realistic flows and geometries is the task of the second step: broadband modeling. Hanson [9] developed the BBCascade code based on Glegg's [13] analytical method. Morin [4] extended it to the BFaNS code using the strip theory. Posson et al. [18,19] and Posson and Roger [20] carried out the analyses based on the analytical cascade response in [14]. Some other models are based on semianalytical harmonic cascade analyses. Rotor–stator interaction (RSI) by Nallasamy and Envia [21] is based on Ventres et al.'s [16] 2-D method. (The most recent RSI results can be found in [22].) Cheong et al. [23] developed a broadband model based on LINSUB [17].

The methods of the next level of fidelity are linear Euler solvers, such as BB3-D code by Atassi and Logue [24]. Recently, there were studies using high-fidelity computational aeroacoustics (CAA) to investigate the interaction noise [3,25,26]. Usually, they were for single-airfoil configurations. For a cascade, a full annulus needs to be modeled, since vorticity waves have different phase lags at the passage periodic boundaries [3]. However, there are still attempts to model a single passage [25].

High-fidelity approaches are computationally intensive, especially in the high-frequency range [22,27]. Although analytical models are computationally efficient, they are limited to single-airfoil configurations and lack of flexibility in applications. For the purpose of conceptual and preliminary designs, a semianalytical model is appropriate, due to easier implementation, faster turnaround computation, and reasonable accuracy. It may also have some degree of flexibility. For example, LINSUB was modified to model gust-perforated cascade response in [27].

This paper is aimed at developing a quasi-3-D model for predicting fan-wake/radial OGV interaction broadband noise. Three-dimensional unsteady lift is calculated using a new semianalytical method. It is then coupled with annular duct modes to obtain in-duct total sound power. Radial variations of the mean flow and geometry are considered in the model. The rest of the paper is arranged as follows. The mechanism of interaction noise is summarized in Sec. II. The prediction approach, the 2-D method, and some important issues are discussed in Sec. III. A 2-D equivalence method for oblique gust/cascade response is introduced in the appendices, based on which the quasi-3-D broadband model is developed in Sec. IV. In Sec. V, the NASA Source Diagnostic Test (SDT) data are postprocessed. Sound power scalings with the vane count and fan speed, are identified and investigated. The test data are then used in Sec. VI to validate the mean flow simulations and the noise predictions using the proposed model. Section VII summarizes the conclusions derived from this study.

II. Mechanism of Fan Broadband Interaction Noise

A. Sound Source

The dominant source is due to vorticity waves in a fan wake interacting with OGVs; a schematic is shown in Fig. 1. Vorticity waves induce upwash velocity at OGV surfaces. Acoustic velocity is generated to negate the upwash velocity to satisfy the impermeable boundary condition at the solid vanes, similar to sound generation by vibrating airfoils. In the acoustic analogy method, unsteady lift on OGVs due to turbulence flow is first computed. It is considered as an equivalent source for far-field sound. However, upwash velocity, and not unsteady lift, is the ultimate driver of the interaction noise.

The frequency and strength of the sound are determined by the upwash velocity. Consider a Fourier component of upwash velocity:

$$\hat{w}(k_1, k_2, k_3)e^{i(k_1\xi + k_2\eta + k_3 z - \omega t)} \tag{1}$$

where ξ and η are the coordinates, respectively, in the chordwise and the chord-normal directions on the reference blade. The spanwise coordinate is z. The wave numbers in the three directions are k_1, k_2, and k_3, respectively. The magnitude is $\hat{w}$. The blades are assumed unloaded, and uniform flow u_0 is in the chordwise direction ξ. To satisfy the linear Euler equations, this dispersion relation must hold for vorticity waves:

$$\omega = k_1 u_0 \tag{2}$$

Circular frequency ω is solely determined by the streamwise wave number of the vorticity wave. The only vorticity waves that generate sound at ω are those with $k_1 = \omega/u_0$. Sound intensity is determined by the upwash velocity magnitude $\hat{w}(k_1, k_2, k_3)$. Turbulence statistics, such as turbulence kinetic energy (TKE) and the dissipation rate ϖ, are readily available from Reynolds-averaged Navier–Stokes (RANS) simulations. To distribute the TKE among eddies of different sizes, an analytical turbulence spectrum has to be used. Three

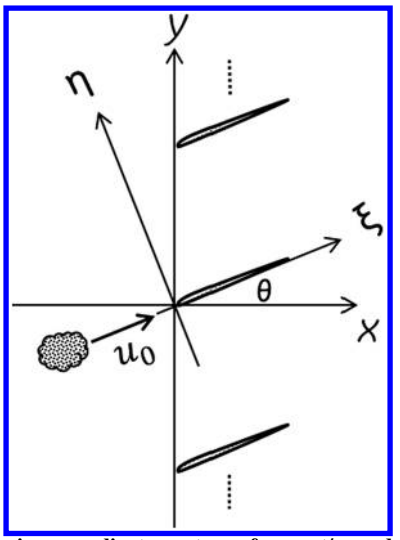

Fig. 1 Cartesian coordinate systems for gust/cascade interaction. (Spanwise coordinate z normal to the paper. No spanwise mean flow.)

[¶]Sutliff, D. L., et al., "Advanced Noise Control Fan II Test Rig Preliminary Design Industry Update," NASA John H. Glen Research Center, 11 Sept. 2012.

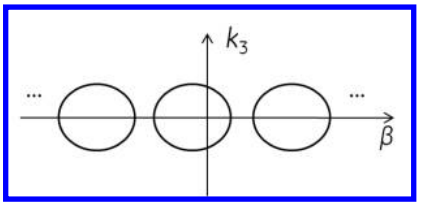

a) Infinite number of ellipses spaced $2\pi/S$ in the vortical wave number space contributing to the cut-on sound

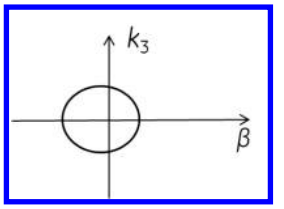

b) The cut-on range in the ellipse in the acoustic wave number space

Fig. 2 Cascade scattering of vorticity waves.

models that are valid for homogeneous and isotropic turbulence flows are available. These are Liepmann, Karman, and Gaussian spectra.

B. Cascade Effects

A cascade affects the sound generation process. Consider a sinusoidal vorticity wave impinging on a cascade. It interacts with the cascade surfaces only at discrete locations (corresponding to the blade positions). The distribution of upwash velocities in the circumferential direction is a periodic series of Dirac delta functions that can be represented by a sum of sine waves [17]. Therefore, a vorticity sine wave is scattered into a number of vorticity sine waves, each of which generates sound. Of these, only a few sound waves can propagate, and they are referred to as "cut on." Figure 2b illustrates the range of wave numbers in the ellipse for cut-on sound waves. These acoustic waves are generated not only by vorticity waves in the same ellipse in the wave number space but also by those in other ellipses spaced apart by $2\pi/S$ due to scattering; see Fig. 2a. (S is the spacing between blades in the cascade.) In the NASA SDT, the vane count B was reduced with the objective to lower broadband noise [28]. However, reducing the vane count reduces the spacing between the ellipses in the vortical wave number space, and hence increases the net energy of sound-generating vortical waves for low vane counts. This, as will be shown later, compensates for the noise reduction due to a reduced number of scattering surfaces (i.e., vanes).

A cascade also affects sound propagation. Acoustic interaction between adjacent blades is strongest at zero stagger in 2-D configurations, where acoustic resonance can lead to large variations in radiated sound power. It is weaker in 3-D due to spanwise variations of gust, flow, and/or geometry (mainly solidity).

C. Effect of Duct

The effect of an annular/cylindrical duct is mainly on sound propagation. Circumferential periodicity and solid-wall boundaries in the radial direction enforce acoustic wave numbers to be discrete instead of a continuous spectrum. The acoustic dispersion relation further restricts the propagating acoustic waves. Waves with higher wave numbers are evanescent (cut off). Only cut-on acoustic waves contribute to the overall radiated sound power, and they are retained in our noise prediction model.

Figure 3 illustrates the relation between vorticity waves and sound waves in the wave number space. The acoustic wave number components in the axial and the unwrapped tangential directions are α and β, respectively (shown as x and y in Fig. 1). The following procedure is used to compute sound power at frequency ω:

1) Identify the vorticity waves contributing to the sound at this frequency using the dispersion relation in Eq. (2). All contributing vorticity wave number vectors must end at the dashed line in Fig. 3.

2) In the tangential direction, acoustic wave numbers $\beta_{aj} = 2\pi j/(BS)$ are discrete (due to circumferential periodicity) and limited to the cut-on range imposed by the duct: integer $j \in [L_{\min}, L_{\max}]$; therefore, vorticity wave numbers $\beta_{vjr} = \beta_{aj} - 2\pi r/S$ are also discrete, shown by the vectors in the figure. (The term with integer r is due to cascade scattering, shown in Fig. 2.)

3) Once the contributing vorticity wave number vectors are identified, their strength is determined by a turbulence energy spectrum, which is modeled analytically. The acoustic response from each vortical wave is then computed, weighted by the turbulence energy it contains, and summed to give the radiated sound power.

III. Prediction Approach and the Two-Dimensional Gust Broadband Model

A. Prediction Approach

The noise prediction includes three steps. First, fan and OGV mean flows are computed using GE Global Research's in-house proprietary computational fluid dynamics (CFD) solver TACOMA, following the procedure described by Sharma et al. [29]. The mean flow is first run in a multistage mode, in which one passage of the rotor and stator blade rows is modeled. A mixing plane is used to exchange circumferentially averaged quantities between the two blade rows. Another mean flow computation is carried out on a finer grid in the fan/OGV gap to convect the fan wake from the fan trailing edge to the OGV leading edge (LE). The output of this step is the circumferentially averaged mean flow, the TKE, and the turbulence dissipation rate ϖ near the OGV LE. The flow, turbulence statistics, and local cascade geometry at each radial location are used in the noise prediction. In the second step, turbulence energy for each vorticity wave is computed using the Liepmann spectrum, and the gust/cascade response is computed either by the LINSUB/Amiet combination method for 2-D gusts or by the 2-D equivalence method for oblique gusts, developed by Ju and Mani [30]. For the 2-D model described in this section, the output is the power spectrum density (PSD) per span. For the quasi-3-D model described in the next section, a third step is carried out to couple unsteady lift at each radial location with annular duct modes to compute in-duct total sound power.

B. Two-Dimensional Prediction Model and Turbulence Spectrum Reduction

The 2-D model is based on the method developed by Cheong et al. [23], with some modifications. The modifications in the current model are the following: 1) the geometry and the mean flow are taken at the midspan; 2) only cut-on modes are included; 3) Amiet's high-frequency response [10] is combined with LINSUB (LINSUB served as a Green's function).

Homogenous and isotropic turbulence is assumed. A study by Grace et al. [22] revealed that the Liepmann spectrum fits the NASA

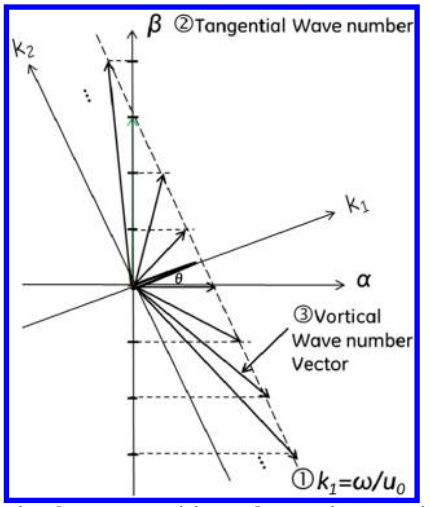

Fig. 3 Relation between vorticity and acoustic waves in the wave number space.

SDT data better in terms of the longitudinal integral length, whereas the Gaussian spectrum fits the lateral integral length better. The large-eddy simulation (LES) by Laborderie et al. [26] showed that the Liepmann spectrum fits the numerical results better. The Liepmann spectrum is adopted in our predictions:

$$\Phi_{ww}(k_1,k_2,k_3)=\frac{2\overline{w^2}\Lambda^3}{\pi^2}\frac{(\Lambda k_1)^2+(\Lambda k_3)^2}{[1+(\Lambda k_1)^2+(\Lambda k_2)^2+(\Lambda k_3)^2]^3} \quad (3)$$

The time-averaged upwash velocity is $w=\sqrt{(2/3)\mathrm{TKE}}$. Λ is the turbulence integral length. To apply Eq. (3) in a 2-D method, some works disregard contributions from oblique gusts ($k_3\neq 0$). The analysis in Sec. IV.A shows that sound is mainly generated by 2-D gusts ($k_3=0$) only when the turbulence integral length is small and duct mode shapes are ignored. Ignoring oblique gust effect usually underpredicts sound power [22]. Another approach, as adopted in [23], is to assume the same cascade response for all k_3. Our study shows that, at a low frequency, unsteady lift (both magnitude and phase) varies little with k_3. (Details are presented in [30].) At a high frequency, the major effect of k_3 is on phase; the variation of magnitude is minimal. Since turbulence energy is concentrated in the low k_3 range [as implied in Eq. (3)], equal response for all k_3 is also used in our 2-D predictions. Then, the energy spectrum in Eq. (3) is integrated over k_3 in the cut-on range as in [9]

$$\Phi_{ww}(k_1,k_2)=\int_{-k_{3\_\mathrm{cuton}}}^{k_{3\_\mathrm{cuton}}}\Phi_{ww}(k_1,k_2,k_3)\,\mathrm{d}k_3 \quad (4)$$

C. Nonsmoothness in Sound Power Spectra

Nonsmoothness in the predicted PSD, as marked in Fig. 4, is typical of 2-D methods that use semianalytical methods. Three types of nonsmoothness can be identified. Small peaks are due to the variation of the number of cut-on modes with frequency. As the frequency increases, the acoustic power factor as defined in equation 21 of Cheong et al. [31] increases, whereas the turbulence energy density and cascade response decrease. Therefore, the total PSD (equal to vorticity wave energy response acoustic power factor) decreases, until, at a frequency, one more mode cuts on. The PSD jumps after this frequency, since more power is added by this cut-on mode. This is illustrated in Fig. 5.

The second type of nonsmoothness in Fig. 4 is the large peaks/valleys in the midfrequency range: sometimes appearing as tones. They are due to cascade resonances, resulting from acoustic interaction between adjacent airfoils. It does not occur in a single-airfoil configuration. The key parameter is the interblade phase angle (IBPA) σ. The IBPA controls how the sources (upwash velocities) at different blades coordinate to generate the sound field. For a zero-stagger cascade, if $\sigma=\pm\pi$, the total velocity at the interface in the middle of the passage is zero. The acoustic field in one passage is exactly the same as a single airfoil vibrating in a wind tunnel. If the wind-tunnel height (i.e., cascade pitch) $S=(m+1/2)\lambda$ (λ: wavelength, $m=0,\pm1,\pm2,\ldots$), the airfoil vibrates with the highest fluctuating velocity and zero lift; sound waves are the cross-section standing waves, which are also called cross-section resonance or Runyan modes [32]. Minimum interference occurs when $\sigma=\pi/2$. Each blade behaves as if it is isolated, and the effective solidity is halved. Similar analysis applies for arbitrary staggers ([33] equations 53a and 53b).

The third type of nonsmoothness seen in Fig. 4 at high frequencies is the erroneous response from LINSUB. A collocation method is used in LINSUB to solve the bound vorticity integral equation. This method is computationally intensive and gives the wrong response at high reduced frequencies.

D. High-Frequency Single-Airfoil Approximation

The erroneous response from LINSUB at high reduced frequencies cannot be eliminated by simply increasing the number of collocation points on the blade. To overcome this limitation, a high-frequency approximation is employed. At low solidity and high frequency, acoustic interactions between the adjacent blades and between the LE and TE on the same blade are weak; therefore, single-airfoil approximations may apply [34]. Asymptotic formulas were developed to take advantage of this feature, such as those for a single airfoil in [11,35,36], for a flat wing with finite span in [37], etc.

Amiet's formula in [35] is adopted in this work. It is used to replace the collocation method in LINSUB to calculate bound vorticity, which is then fed into LINSUB to compute the acoustic field. LINSUB serves as a Green's function in this LINSUB/Amiet combination method. A

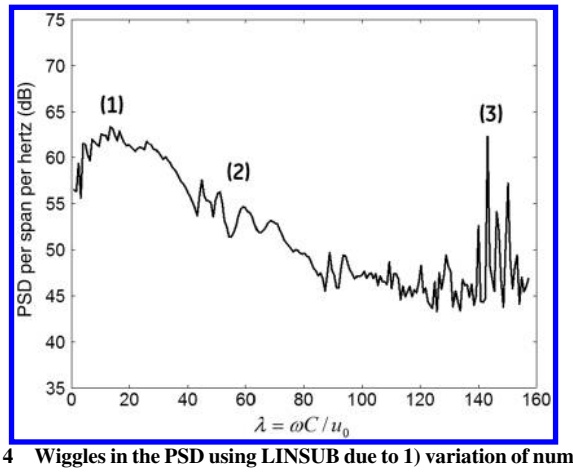

Fig. 4 Wiggles in the PSD using LINSUB due to 1) variation of number of cut-on modes, 2) cascade resonance, and 3) erroneous response.

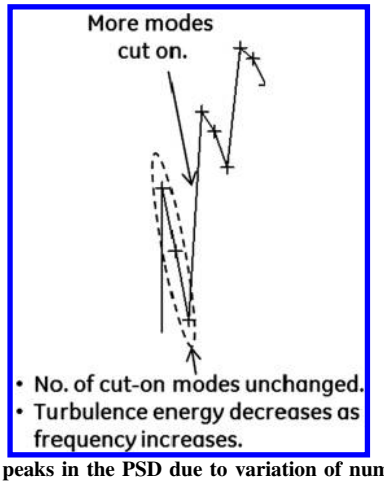

Fig. 5 Small peaks in the PSD due to variation of number of cut-on modes with frequency.

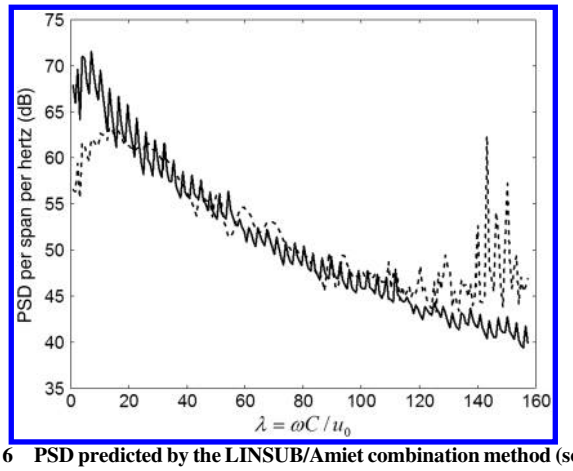

Fig. 6 PSD predicted by the LINSUB/Amiet combination method (solid line) and LINSUB (dashed line).

result using this approach is shown in Fig. 6. The erroneous response at high frequency is eliminated. The result matches the LINSUB well, except at very low frequency. The single-airfoil approximation is valid for $M\lambda/(1-M^2)>\pi/2$, where reduced frequency $\lambda = \omega C/u_0$ [35]. The frequency above which the approximation is valid for cascades is higher: $M\lambda/(1-M^2) > 5$ for the upstream PSD and $M\lambda/(1-M^2) > 20$ for the downstream PSD for the test case in Fig. 6.

E. Modeling of Turbulence Statistics

Turbulence in fan wakes is not periodic between cascade passages. However, turbulence statistics (TKE and Λ) are periodic. Nallasamy and Envia [21] model this periodicity by separating wake turbulence from background turbulence. The two turbulence components (wake and background) are assumed uncorrelated. The wake TKE is modeled as a periodic train of Gaussian functions. Uniform length scales are used for both the background and wake turbulence. Jurdic et al. [38], Soulat et al. [39], Dieste and Gabard [40], and Posson et al. [18] followed the same approach.

Tones are generated by a mean velocity deficit interacting with the OGVs. The mean velocity profile must be modeled to predict tones. However, for broadband noise, OGVs experience randomly varying upwash velocity, even though the turbulence statistics are periodic. A typical turbulence length scale in the SDT is about 5% of the span of a fan blade, which is smaller than the pitch of a typical OGV cascade. Therefore, the correlation of upwash velocity between vanes is small. It may suffice to use circumferentially averaged turbulence in broadband noise predictions for high-BPR engines. In the SDT data, no strong peaks were found around the blade-passing frequency (BPF) and its harmonics in the broadband noise spectra. This is the evidence of small turbulence scales in fan wakes.

In Eq. (3), the energy of each vorticity wave is linearly proportional to the TKE and nonlinearly related to Λ. The TKE is additive as long as Λ is uniform in the cascade passage. This explains why modeling the circumferential distribution of the TKE is not needed. What matters is the total or the averaged TKE in the wake. Structures of turbulence statistics (periodicity, wake width, etc.) have little effect as long as the integral length scale is uniform. Similar conclusion can be inferred from figures 15, 16, and 20 in [40], as well as from RSI results in [22,41]. Figure 7 compares the PSD spectra using different wake turbulence models. There is little difference between the results using the averaged TKE and the Gaussian distributed TKE.

The integral length scale Λ has a significant impact on the shapes of the turbulence spectra and PSD, shown in Fig. 8. It is necessary to model integral length scales in the background and in the wake separately. Therefore, this simple model is recommended:

1) The background and wake turbulence are modeled separately.

2) For each, the circumferentially averaged TKE and integral length scale are used.

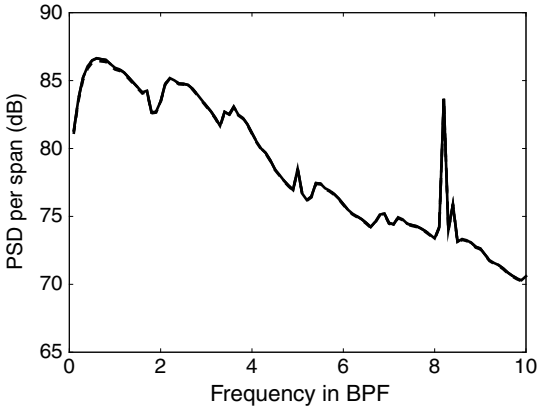

Fig. 7 PSD using different wake turbulence models ($\Lambda = 3.95$ mm in background and wake): averaged TI = 1.38% used in both wake and background (dotted line); background TI = 1% and wake TI = 0.96% (solid line); wake turbulence structure modeled as in Eq. (29) in [38], background TI = 1%, wake peak TI = 2%, and Gaussian half – width = 14.6%S (dashed line).

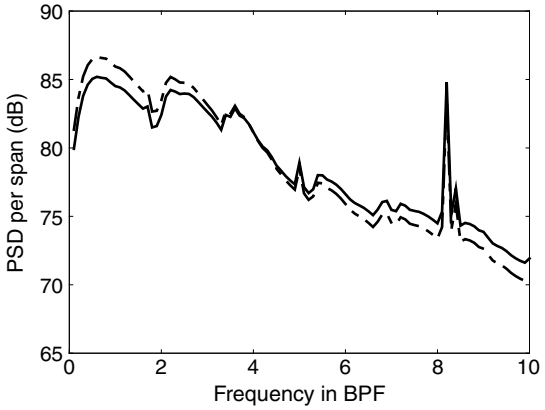

Fig. 8 Effect of turbulence integral length Λ on PSD spectrum shape: $\Lambda = 3.95$ mm in background and wake (dashed line); and $\Lambda = 2$ mm in background and 3.95 mm in wake (solid line).

IV. Quasi-Three-Dimensional Gust Broadband Model in Annular Duct

A quasi-3-D broadband model is developed in this paper. Radial distributions of mean flow and geometry are considered based on the strip theory. Unsteady lift on blade surfaces due to oblique gust–linear cascade interaction is computed using the 2-D equivalence method. It is coupled with annular duct modes to obtain noise power in the exhaust duct. The detailed derivation of the PSD [Eq. (C8)] is given in Appendix C. Radial turbulence integral lengths and their impact on the predicted PSD are discussed in this section.

A. Sound Power Spectrum in Uniform Flow

Since the cross-power spectral density $\Phi_{ww}(k_1,k_2,k_3)$ for homogeneous turbulence is used in the broadband model, the integration range of Δr in Eq. (C8) must be near r. This restriction can be removed if the mean flow and the turbulence statistics are uniform. Then, Eq. (C8) becomes

$$\langle \hat{W}^{\pm}_{mn}\rangle = \pm\frac{B}{4\rho_d a_d \Gamma_{mn}\kappa_{mn}}\frac{k_d(1-M_d^2)^2}{(k_d \mp M_d\kappa_{mn})^2} \times \mathrm{Real}\left\{\int_{R_i}^{R_o}\frac{u_0\rho_0^2}{S\cos\theta}\Psi^*_m(\mu_{mn}r)\int_{-\infty}^{\infty}\left|\hat{h}^{\pm}_{mn}\left(K_1,\frac{2\pi m}{BS\cos\theta}-K_1\tan\theta,k_3\right)\right|^2 \times\left[\sum_{j=-\infty}^{\infty}\Phi_{ww}\left(K_1,\frac{2\pi(m+Bj)}{BS\cos\theta}-K_1\tan\theta,k_3\right)\right]\times \int_{R_i-r}^{R_o-r}\Psi_m(\mu_{mn}(r+\Delta r))e^{-ik_3\Delta r}\,\mathrm{d}\Delta r\,\mathrm{d}k_3\,\mathrm{d}r\right\} \quad (5)$$

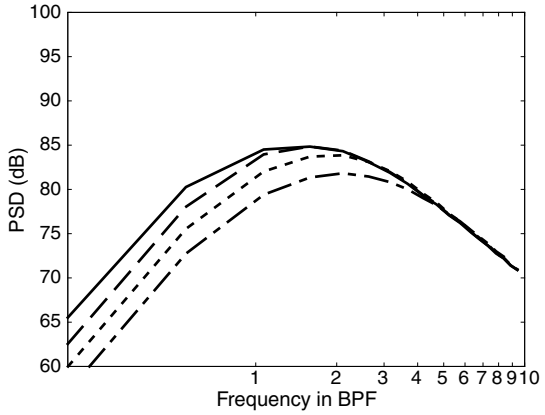

Fig. 9 Impact of integration range on predicted PSD. NASA SDT at approach: $L_r = 5\%$ span (dashed–dotted line), $L_r = 10\%$ span (dotted line), $L_r = 20\%$ span (dashed line), and $L_r = 100\%$ span (solid line).

No strip assumption is needed, and the numerically exact sound power can be obtained from this equation. Examining its integrand and ignoring the duct mode shape for the time being, one may find integration

$$\int_{R_i-r}^{R_o-r} \hat{F}(k_1,k_2,\Delta r)\,\mathrm{d}\Delta r$$

$\hat{F}(k_1,k_2,\Delta r)$ is the spanwise cross correlation of unsteady lift:

$$\hat{F}(k_1,k_2,\Delta r) \equiv \int_{-\infty}^{\infty} \hat{h}^{\pm}_{mn}(k_1,k_2,k_3)\hat{h}^{\pm *}_{mn}(k_1,k_2,k_3) \times \sum_{j=-\infty}^{\infty} \Phi_{ww}\left(k_1,k_2+\frac{2\pi j}{S\cos\theta},k_3\right)e^{-ik_3\Delta r}\,\mathrm{d}k_3$$

Its correlation length is

$$L_f \equiv \int_0^{\infty} \hat{F}(k_1,k_2,\Delta r)\,\mathrm{d}\Delta r/\hat{F}(k_1,k_2,0)$$

If L_f is finite, the integration range of Δr in Eq. (5) can be reduced from (R_i-r, R_o-r) to $(-L_r, L_r)$ or (L_1, L_2), as long as $L_r \gg L_f$:

$$L_1 = \max(-L_r, R_i-r), L_2 = \min(L_r, R_o-r) \tag{6}$$

Figure 9 depicts the impact of L_r on PSD accuracy. At low frequency, the computed sound power increases with the integration limit, indicating that the integration is not converged. As L_r increases, the PSD approaches the numerically exact result from the full span integration. A small L_r gives reasonable accuracy only at high frequency. At low frequency, the PSD is underpredicted; larger L_r is needed to achieve accuracy. For the SDT data at approach [42], our study found $L_r \sim 8\Lambda$ is suitable for the baseline OGV configuration in the entire frequency range. $L_r = 0.5\Lambda$, adopted in some studies, works only in the high-frequency range.

If L_r is small and mode shapes vary little within the integration range, then in a region away from the duct walls,

$$\int_{R_i-r}^{R_o-r} \Psi_m(\mu_{mn}(r+\Delta r))e^{-ik_3\Delta r}\,\mathrm{d}\Delta r \approx \Psi_m(\mu_{mn}r)\int_{-\infty}^{\infty} e^{-ik_3\Delta r}\,\mathrm{d}\Delta r = 2\pi\Psi_m(\mu_{mn}r)\delta(k_3)$$

Noise is mainly generated by 2-D gusts ($k_3 = 0$). Contributions from oblique gusts cancel each other. It is not the case for high radial modes, for regions near the duct walls, or for large turbulence length scales.

B. Sound Power Spectrum in Nonuniform Flow

If the mean flow and the turbulence statistics are not uniform, the integration limits of Δr in Eq. (C8) must be small so that the analytical turbulence spectrum is applicable and the computation of response can be simplified as):

$$\langle \hat{W}^{\pm}_{mn}\rangle = \pm\frac{B}{4\rho_d a_d \Gamma_{mn}\kappa_{mn}}\frac{k_d(1-M_d^2)^2}{(k_d \mp M_d\kappa_{mn})^2} \times \mathrm{Real}\left\{\int_{R_i}^{R_o}\frac{u_0\rho_0^2}{S\cos\theta}\Psi^*_m(\mu_{mn}r)\int_{-\infty}^{\infty}\left|\hat{h}^{\pm}_{mn}\left(K_1,\frac{2\pi m}{BS\cos\theta}-K_1\tan\theta,k_3|r\right)\right|^2 \times\left[\sum_{j=-\infty}^{\infty}\Phi_{ww}\left(K_1,\frac{2\pi(m+Bj)}{BS\cos\theta}-K_1\tan\theta,k_3\right)\right] \times\int_{L_1}^{L_2}\Psi_m(\mu_{mn}(r+\Delta r))e^{-ik_3\Delta r}\mathrm{d}\Delta r\,\mathrm{d}k_3\,\mathrm{d}r\right\} \tag{7}$$

Equation (7) is used in our predictions. In theory, the integrations should yield a real number. It is not guaranteed with numerical implementations. Therefore, the real part is taken to obtain $\hat{W}^{\pm}_{mn}$. The integration over r may be continuous; no strip theory is needed. The integration over Δr should be carried out in a narrow strip. The criteria of choosing range (L_1, L_2) are 1) large enough to ensure integration convergence, and 2) as small as possible to ensure flow uniformity. The first criterion is important. Our study shows that we would rather have a wider integration range to ensure integration convergence, even if the requirement of flow uniformity is not met.

C. Spanwise Turbulence Integral Lengths and Integration Limits

To make Eq. (7) valid, at any radial location r, the flow and turbulence must be approximately uniform within integration range (L_1, L_2). This range must be much larger than radial correlation length L_f of unsteady lift so that the integration converges; and it must be as narrow as possible to ensure flow uniformity. The key is to find L_f. The NASA SDT data show that the unsteady pressure field is essentially homogeneous, with only a modest variation across the vane [43]. The unsteady pressure integral length is about four times the turbulence lateral integral length. The LES results in [26] also reveal a larger unsteady pressure length scale. There is little work in the literature on modeling this length scale.

There are reasons to believe that the turbulence integral length can be used to estimate the integration range. As we have mentioned earlier, the upwash velocity on airfoils induced by turbulence flow is the ultimate sound source. The study in [30] shows that the cascade response function $\hat{h}^{\pm}_{mn}(k_1,k_2,k_3)$ depends on k_3 weakly. This simplification applies:

$$\int_{-\infty}^{\infty}\int_{-\infty}^{\infty}\hat{h}^{\pm}_{mn}(k_1,k_2,k_3|r)\hat{h}^{\pm *}_{mn}(k_1,k_2,k_3|r+\Delta r) \times\sum_{j=-\infty}^{\infty}\Phi_{ww}\left(k_1,k_2+\frac{2\pi j}{S\cos\theta},k_3\right)e^{-ik_3\Delta r}\,\mathrm{d}k_3\,\mathrm{d}\Delta r \sim\int_{-\infty}^{\infty}\hat{h}^{\pm}_{mn}(k_1,k_2,k_3=0|r)\hat{h}^{\pm *}_{mn}(k_1,k_2,k_3=0|r+\Delta r) \times\sum_{j=-\infty}^{\infty}\left\langle\hat{w}\left(k_1,k_2+\frac{2\pi j}{S\cos\theta},r\right)\hat{w}^*\left(k_1,k_2+\frac{2\pi j}{S\cos\theta},r+\Delta r\right)\right\rangle d\Delta r \tag{8}$$

For the Liepmann spectrum [Eq. (3)],

$$\langle\hat{w}(k_1,k_2,r)\hat{w}^*(k_1,k_2,r+\Delta r)\rangle = \int_{-\infty}^{\infty}\Phi_{ww}(k_1,k_2,k_3)e^{-ik_3\Delta r}\mathrm{d}k_3 = \frac{\overline{w^2(t)}}{4\pi[1+(\Lambda k_1)^2+(\Lambda k_2)^2]^{5/2}}e^{-\sqrt{1+(\Lambda k_1)^2+(\Lambda k_2)^2}|\Delta r|/\Lambda} \cdot\{\Lambda[1+4(\Lambda k_1)^2+(\Lambda k_2)^2] \cdot[\Lambda+\sqrt{1+(\Lambda k_1)^2+(\Lambda k_2)^2}|\Delta r|]-[1+(\Lambda k_2)^2] \times[1+(\Lambda k_1)^2+(\Lambda k_2)^2]\Delta r^2\}$$

The spanwise turbulence integral length scale is

$$L'_T \equiv \int_0^{\infty}\int_{-\infty}^{\infty}\Phi_{ww}(k_1,k_2,k_3)e^{-ik_3\Delta r}\,\mathrm{d}k_3\,\mathrm{d}\Delta r/\int_{-\infty}^{\infty}\Phi_{ww}(k_1,k_2,k_3)\,\mathrm{d}k_3 = \frac{8\Lambda(\Lambda k_1)^2}{[1+4(\Lambda k_1)^2+(\Lambda k_2)^2]\sqrt{1+(\Lambda k_1)^2+(\Lambda k_2)^2}} \tag{9}$$

If $\Delta r \gg L'_T$, $\langle\hat{w}(k_1,k_2,r)\hat{w}^*(k_1,k_2,r+\Delta r)\rangle$ approaches zero. L'_T is different from the classic turbulence lateral length scale:

$$L_C = \int_0^\infty \langle w(\xi,\eta,r)w^*(\xi,\eta,r+\Delta r)\rangle \,\mathrm{d}\Delta r / \langle w(\xi,\eta,r)w^*(\xi,\eta,r)\rangle \approx \Lambda/2 \tag{10}$$

It is also different from the length scale for the single-airfoil response defined in [10] and adopted in [18]:

$$L_A \equiv \int_0^\infty \int_{-\infty}^\infty \int_{-\infty}^\infty \Phi_{ww}(k_1,k_2,k_3)\,\mathrm{d}k_2 e^{ik_3\Delta r}\,\mathrm{d}k_3\,\mathrm{d}\Delta r / \times \int_{-\infty}^\infty \int_{-\infty}^\infty \Phi_{ww}(k_1,k_2,k_3)\,\mathrm{d}k_2\,\mathrm{d}k_3 = \Lambda \frac{3\pi(K_1\Lambda)^2}{2\sqrt{1+(K_1\Lambda)^2}[1+3(K_1\Lambda)^2]} \tag{11}$$

The integration over k_2 in this definition accounts for the contribution to broadband noise from all the vorticity waves with the same k_1 and k_3. For the cascade response, only a discrete number of vorticity waves contributes to broadband noise, shown by the summation over j in Eq. (8). We choose the maximum L_T' for all k_2 in Eq. (9), as it is more conservative to ensure integration convergence:

$$L_T'' \equiv \Lambda \frac{8(\Lambda k_1)^2}{[1+4(\Lambda k_1)^2]\sqrt{1+(\Lambda k_1)^2}} \geq L_T' \tag{12}$$

The four length scales are compared in Fig. 10. Figure 11 is the predicted PSD for the SDT at the approach condition using the integration limit L_r equal to eight times the length scales. L_T'' and L_A are better at high frequency. L_C is better at low frequency. L_T, defined in Eq. (13) and shown in Fig. 12, is modified from L_T'' to improve the PSD accuracy at low frequency. $L_r = 8L_T$ is used as the radial integration limit in our study:

$$L_T/\Lambda = \begin{cases} 1.136 - 0.755(\Lambda k_1 - 0.918)^2, & \Lambda k_1 \leq 0.918; \\ \frac{8(\Lambda k_1)^2}{[1+4(\Lambda k_1)^2]\sqrt{1+(\Lambda k_1)^2}}, & \Lambda k_1 > 0.918 \end{cases} \tag{13}$$

V. NASA Source Diagnostic Test Data Analysis

The NASA SDT data reported in [42] are used to validate the proposed noise prediction methodology. Two rotors (R4 and M4) were tested in the SDT campaign. Only the R4 rotor data were used for the validation. Noise measurements were made with and without the OGVs present. In the "fan-alone" configuration (OGVs removed), a vane nozzle with variable area was used to ensure running of the fan at the same operating condition as in the "stage" configuration (OGVs present). Noise data were acquired for each set of OGVs in these two configurations so as to isolate different fan noise sources. It was expected that the fan-alone configuration would give fan self-noise and, through subtraction of these from stage configuration measurements, interaction noise could be identified. Furthermore, measurements were made with and without an aft barrier intended to shield aft-radiated noise. With the aft barrier in place, only the inlet-radiated noise would be measured.

Fan exhaust broadband noise associated with fan-wake/OGV interaction is extracted from the test data using the following procedure:

1) Tones are first removed from the full spectra.

2) Inlet-radiated noise (measured with the aft barrier in place) is then subtracted from measurements without the barrier.

3) Fan self-noise (measured in the fan-alone configuration) is subtracted out from stage measurements. This procedure to isolate the interaction noise source, however, met with limited success. The measurements reported higher noise in the fan-alone configuration than in the corresponding stage configuration. This anomaly was observed for almost the entire spectra at takeoff and cutback conditions, as well as for low (less than 0.75 BPF) and high (greater than 7 BPF) frequencies at the approach condition (see Fig. 13). The validation is therefore limited to the midfrequency range at the approach condition where meaningful exhaust radiated noise data are available.

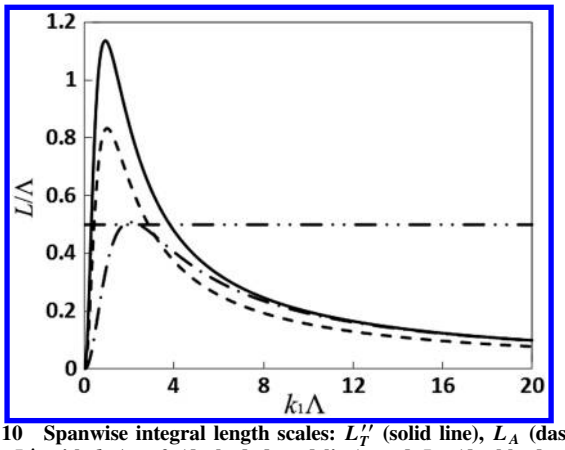

Fig. 10 Spanwise integral length scales: L_T'' (solid line), L_A (dashed line), L_T' with $k_2\Lambda = 2$ (dashed–dotted line), and L_C (double dotted–dashed line).

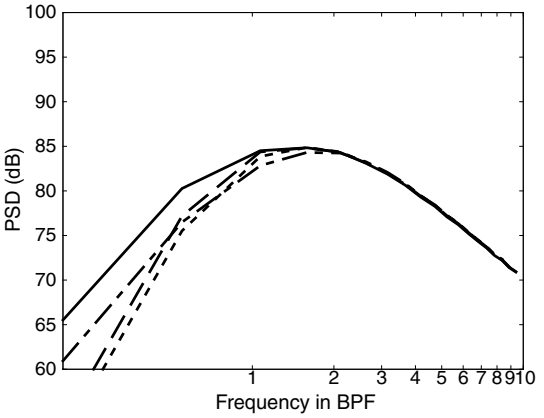

Fig. 11 Effects of using different length scales in the integration limit: full span integration (solid line), $L_r = 8L_C$ (dashed–dotted line), $L_r = 8L_T''$ (dashed line), and $L_r = 8L_A$ (dotted line).

The postprocessed data are next used to study the scaling laws of interaction broadband noise in the SDT. Sound power at approach with and without vane count scaling is shown in Fig. 14. At frequencies below the BPF, noise levels are almost the same for the two vane counts. At frequencies above 2.5 BPF, the linear vane count scaling collapses the data well. The effect of the tip Mach number on the PSD is examined in Fig. 15. The PSD subtracted by 10 $\log(M_T^{3.3})$ yields a good data collapse.

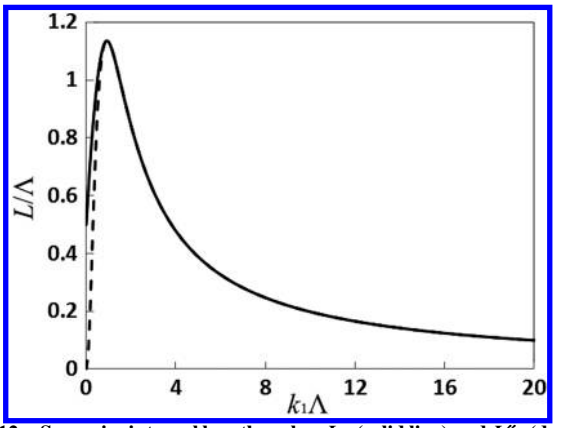

Fig. 12 Spanwise integral length scales: L_T (solid line) and L''_T (dashed line).

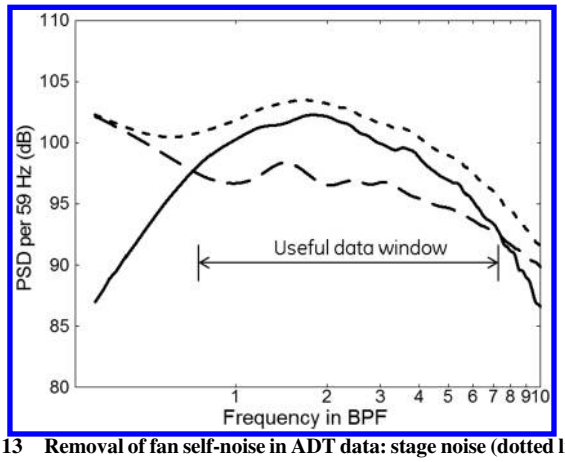

Fig. 13 Removal of fan self-noise in ADT data: stage noise (dotted line), fan-alone noise (dashed line), and fan-alone noise subtracted from stage noise (solid line).

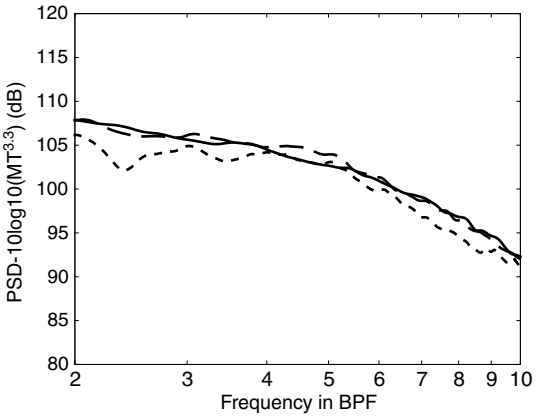

Fig. 15 NASA SDT exhaust-radiated fan/OGV interaction noise data at approach: $B = 54$. Speed scaling of $M_T^{3.3}$ collapses the data well: approach (solid line), cutback (dashed line), and takeoff (dotted line).

VI. Validation

The proposed prediction methodology is applied to two vane count configurations at three operating conditions in the SDT campaign. Comparisons with the test data are made to assess the accuracy of the approach in predicting absolute noise levels, as well as trends with vane count and fan speed.

A. Mean Flow and Turbulence Statistics

Accurate predictions of mean flow and turbulence statistics near the OGV leading edges are critical. Grace et al. [41] studied the sensitivity of the RSI software to mean flow inputs, and they found that the background turbulence intensity and integral length scale have the biggest impact. In the current study, the total pressure (PT), total temperature (TT), and flow angle are specified at the inlet boundary. CFD simulations are tuned to match the measured exit-corrected flow rates. The PT and TT from the simulations are circumferentially averaged at the location of the PT/TT rakes in the test. Figure 16 shows good agreement between the simulation and the test data at the approach condition [44]. Similar agreements are observed at cutback and at takeoff.

A mixing plane approach is used in the multistage RANS calculations [29]. Flow details in the fan wake are averaged out at the mixing plane. To obtain fan-wake information at the OGV leading edge, follow-up simulations are performed to convect the fan wake from the fan trailing edge to the OGV leading edge. Radial profiles of circumferentially averaged TKE and ϖ are extracted at the OGV leading-edge locations. The fluctuating velocity for isotropic turbulence is $w = \sqrt{(2/3)\text{TKE}}$. The turbulence integral length scale is approximated by

$$\Lambda \approx 10\sqrt{\text{TKE}}/\varpi \tag{14}$$

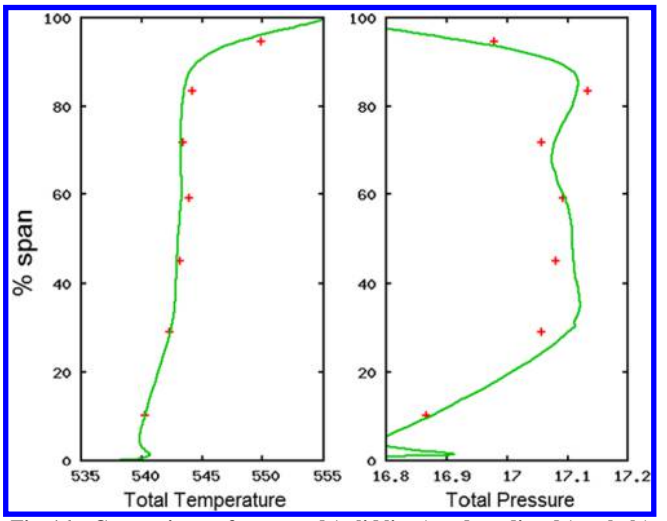

Fig. 16 Comparisons of measured (solid lines) and predicted (symbols) mean flow profiles at the rake location: approach condition. SDT data from [44].

similar to [41]. (Refer to [45] for details evaluating the integral length scales.)

Figure 17 compares the root mean square (RMS) of the measured and predicted axial and circumferential components of fluctuating velocity at two axial locations downstream of the fan (denoted by Laser Doppler Velocimetry (LDV)1 and LDV2). The measured axial and tangential fluctuating velocities are approximately equal (especially at LDV1), justifying the assumption of isotropic turbulence made in the proposed prediction procedure. The RANS simulations underpredict turbulence intensity and dissipation rate.

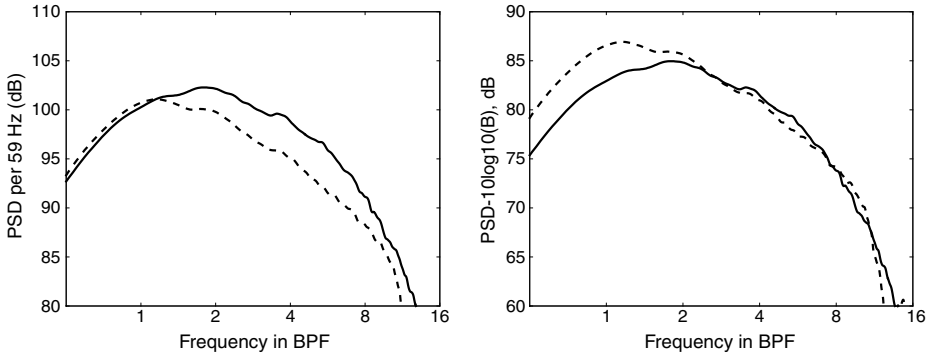

a) Without vane count scaling **b) With $10\log_{10}(B)$ scaling**

Fig. 14 NASA SDT exhaust-radiated fan/OGV interaction noise data at approach: $B = 54$ (solid line) and $B = 26$ (dashed line).

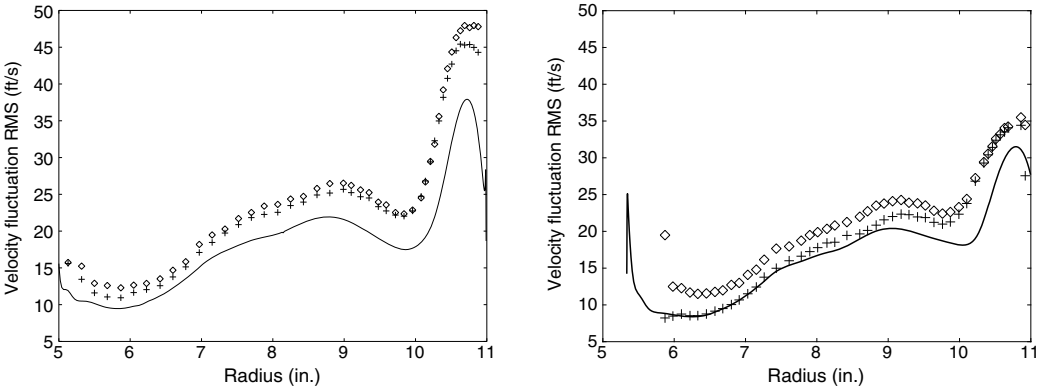

a) At LDV1 (3.12 in. downstream of fan tip trailing edge) b) At LDV2 (6.49 in. downstream of fan tip trailing edge)

Fig. 17 RMS of measured and predicted axial and tangential components of fluctuating velocity at approach condition: simulation (solid line), axial fluctuating velocity in LDV data (diamonds), and tangential fluctuating velocity in LDV data (+ symbols). LDV data from [46].

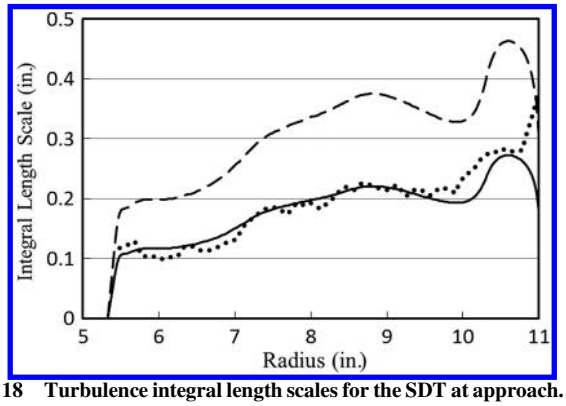

Fig. 18 Turbulence integral length scales for the SDT at approach. The location in the simulation is 0.33 in. upstream of the hotwire Hot wire 2 (HW2) in the test: streamwise integral length from HW2 in test (dotted line), simulation (dashed line), and simulation with correction (solid line).

But, at LDV2, the simulated upwash velocity is close to the tangential fluctuating velocity in the test. The simulated turbulence intensity is used in the noise prediction without any correction.

The ratio of the integral length scales in the streamwise and the chord-normal directions is roughly 2 between 20 and 80% of the span (see figure 25 in [46]), further justifying the isotropic turbulence assumption. Figure 18 compares predicted [using Eq. (14)] versus measured streamwise integral length scales. The prediction overestimates the integral length almost by a factor of two. This is corrected by scaling it down by a factor of 1.7 (see Fig. 18) before use with the proposed noise prediction process.

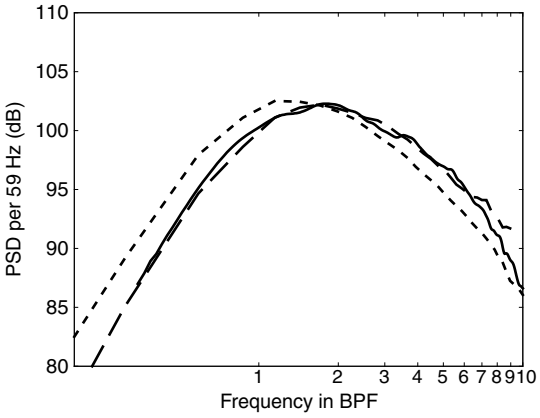

Fig. 19 PSD predictions compared with NASA SDT data at the approach condition: test data (solid line), prediction using 2-D equivalence method with LINSUB (dashed line), and prediction using 2-D equivalence method with high-frequency single-airfoil approximation (dotted line).

B. PSD Comparison

The midspan vane chord is used in the cascade response calculations. The effect of vane twist is modeled through radial variation of the stagger angle. The airfoil camber and thickness are ignored. The current model cannot capture the effects of swirling flow and the fan cascade on noise transmission, which are needed to predict inlet radiated noise [47]. Neither can it account for acoustic reflection from the fan cascade. The focus is therefore limited to exhaust noise directly radiated from the OGV. Figure 19 compares the measured exhaust noise PSD against predictions made using the 2-D equivalence method with LINSUB. Very good agreement is observed. The prediction using the 2-D equivalence method with the high-frequency single-airfoil approximation (described in Sec. III.D) is also shown. As explained in Appendix A, $\bar{M}\bar{\lambda}/(1-\bar{M}^2) > \pi/2$ is not satisfied in the 2-D equivalence method, even at high frequency when k_3 approaches the cutoff condition. And, the vane count is so large that the cascade effect cannot be ignored. Therefore, the predicted spectrum does not converge on that using LINSUB. However, it does a good job of capturing the spectrum shape in this case.

C. Vane Count Trend

A general form of vane count scaling is written as

$$\mathrm{PSD}_1 - \mathrm{PSD}_2 = 10\log_{10}(B_1/B_2)^{\mu} \tag{15}$$

The 2-D broadband model in [23] predicts $\mu = 1$ at high frequency. Chord C is held fixed in [23]. Also, $\mu = 2$ has been suggested by others (see, e.g., [21] and Eq. (186) in [16]). The NASA SDT data shown in Fig. 14 exhibit two vane count trends: $\mu \sim 0$ at low frequency, and $\mu = 1$ at high frequency. The Boeing 18 in. Low-Speed Aeroacoustic Facility data show $\mu < 1$ [5]. In [5,16,21], the vane solidity C/S is held fixed, which is the right metric to hold constant from geometric and dynamic scaling perspectives.

Examining Eq. (7) reveals that the sound power (per span and per k_3) is roughly proportional to the vane count, turbulence energy per pitch, and chordwise integrated response squared:

$$\langle \hat{W}^{\pm}_{mn} \rangle \sim B \cdot \frac{1}{S} \sum_{j=-\infty}^{\infty} \Phi_{ww}\left(K_1, \frac{2\pi(m+Bj)}{BS\cos\theta} - K_1 \tan\theta, k_3\right) \cdot \left|\hat{h}^{\pm}_{mn}\left(K_1, \frac{2\pi m}{BS\cos\theta} - K_1\tan\theta, k_3\right)\right|^2 \tag{16}$$

Figure 20 illustrates typical variations of

$$\sum \Phi_{ww}/S$$

at the SDT approach condition.

$$\sum \Phi_{ww}/S$$

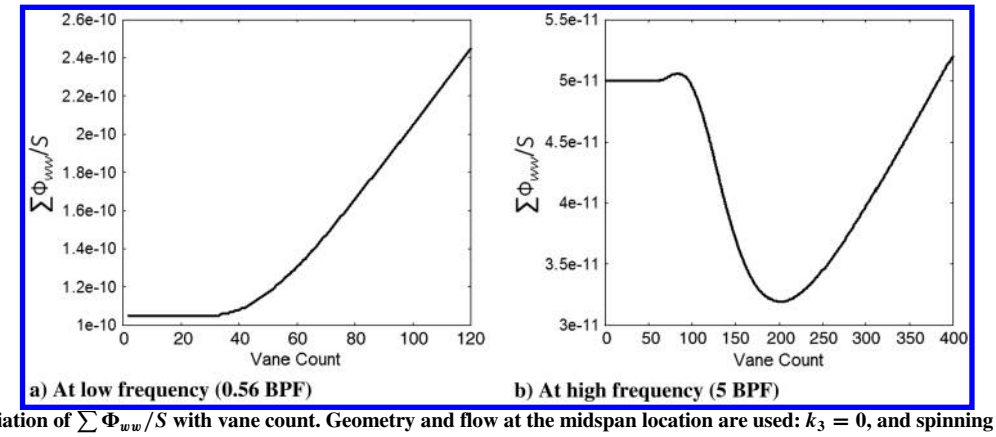

Fig. 20 Variation of $\sum \Phi_{ww}/S$ with vane count. Geometry and flow at the midspan location are used: $k_3 = 0$, and spinning mode $m = 0$.

may be considered as the numerical integration of Φ_{ww} with interval $\Delta t = 1/S$:

$$I \equiv \int_{-\infty}^{\infty} \Phi_{ww}\left(K_1, \frac{2\pi m}{BS\cos\theta} + \frac{2\pi}{\cos\theta}t - K_1\tan\theta, k_3\right) \mathrm{d}t$$
$$\approx \Delta t \sum_{j=-\infty}^{\infty} \Phi_{ww}\left(K_1, \frac{2\pi m}{BS\cos\theta} + \frac{2\pi}{\cos\theta}j\Delta t - K_1\tan\theta, k_3\right)$$
$$= \frac{1}{S}\sum_{j=-\infty}^{\infty} \Phi_{ww}\left(K_1, \frac{2\pi(m+Bj)}{BS\cos\theta} - K_1\tan\theta, k_3\right)$$

When B is smaller than a critical value B_c, Φ_{ww} is a smooth function with regard to its second argument. Integral I can also be numerically integrated using $\Delta t = 1/(BS)$:

$$I \approx \frac{1}{BS}\sum_{j=-\infty}^{\infty} \Phi_{ww}\left(K_1, \frac{2\pi m}{BS\cos\theta} + \frac{2\pi}{BS\cos\theta}j - K_1\tan\theta, k_3\right)$$

Therefore, this approximation applies:

$$\frac{1}{S}\sum_{j=-\infty}^{\infty} \Phi_{ww}\left(K_1, \frac{2\pi(m+Bj)}{BS\cos\theta} - K_1\tan\theta, k_3\right)$$
$$\approx \frac{1}{BS}\sum_{j=-\infty}^{\infty} \Phi_{ww}\left(K_1, \frac{2\pi(m+j)}{BS\cos\theta} - K_1\tan\theta, k_3\right)$$

$\sum \Phi_{ww}/S$ varies little with vane count, since BS is a constant. This is consistent with Eq. (35) in [23]. When $B > B_c$,

$$\sum \Phi_{ww}/S$$

varies nonlinearly for moderate values of B. For very large B, it increases linearly with B. B_c increases with frequency. At the SDT approach condition, $B_c = 25$ at 0.56 BPF and $B_c = 65$ at 5 BPF.

The variation of $\hat{h}^{\pm}_{mn}$ depends on many factors. To simplify the analysis, we study

$$\hat{h}^{+}_{s} = \sqrt{\sum |\hat{h}^{+}_{mn}|^2}$$

with the summation carried out over all cut-on modes. If C is kept constant, the IBPA and solidity vary with B, whereas the other three input parameters to LINSUB (stagger angle θ, Mach number, and reduced frequency λ) are unchanged. Figure 21a illustrates the variation of $\hat{h}^{+}_{s}$ at low frequency. When $S/C > 2.7 (B < 12)$, the acoustic interaction between blades is small; $\hat{h}^{+}_{s}$ converges on the single-airfoil approximation. When B is large (greater than 54 in Fig. 21a), the response is inversely proportional to B (refer to the dotted line in the figure). Similar trends are found in Fig. 21b for high frequency. Also, $\hat{h}^{+}_{s}$ is inversely proportional to B for $B > 100$. It approaches the single-airfoil approximation when $B < 25$. It changes drastically for $25 < B < 100$.

Solidity is kept fixed in the SDT for aerodynamic scaling. C, the IBPA, and λ increase as B reduces. (The PSD spectrum shift toward lower frequency would be expected.) Variations of $\hat{h}^{+}_{s}$ with λ at low frequency are shown in Fig. 22a. The single-airfoil response barely changes for $\lambda > 10$ and $B < 27$. It does not increase with λ or chord, indicating leading-edge dominance of unsteady lift. It is not the case for the cascade response. The cascade effect does not decrease with B due to the increasing chord. For small B (less than four), $\hat{h}^{+}_{s}$ scales with C or λ. For large B (greater than 11), $\hat{h}^{+}_{s}$ scales approximately with $\sqrt{C}$ or $\sqrt{\lambda}$. A strong cascade effect also occurs at high frequency (Fig. 22b). In the high reduced frequency range, $\hat{h}^{+}_{s}$ is fitted by a square root line. When B is very large (greater than 128), $\hat{h}^{+}_{s}$ varies smoothly and scales with $\sqrt{C}$ or $\sqrt{\lambda}$. Figure 22 reveals that the cascade response does not approach the single-airfoil response when solidity is maintained.

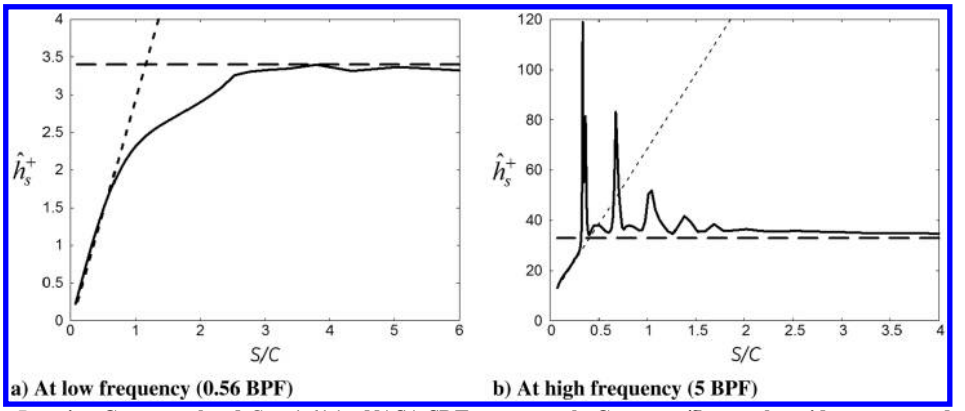

Fig. 21 $\hat{h}^{+}_{s}$ vs S/C as B varies. Constant chord $C = 1.61$ in. NASA SDT at approach. Geometry/flow at the midspan are used, with $k_3 = 0$: cascade response (solid line), single-airfoil response (dashed line), and linearly fitted curve for small S/C (dotted line).

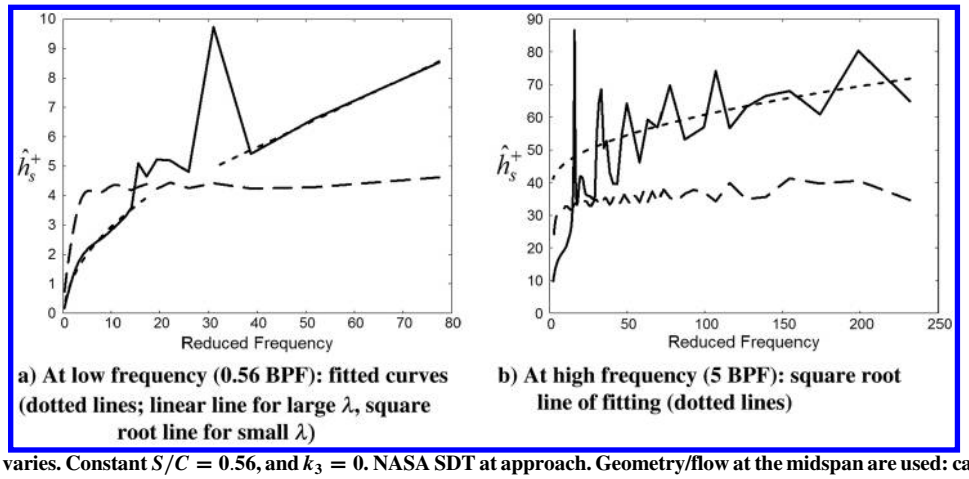

a) At low frequency (0.56 BPF): fitted curves (dotted lines; linear line for large λ, square root line for small λ)

b) At high frequency (5 BPF): square root line of fitting (dotted lines)

Fig. 22 $\hat{h}_s^+$ **vs** λ **as** B **varies. Constant** $S/C = 0.56$**, and** $k_3 = 0$**. NASA SDT at approach. Geometry/flow at the midspan are used: cascade response (solid line), and single-airfoil response (dashed line).**

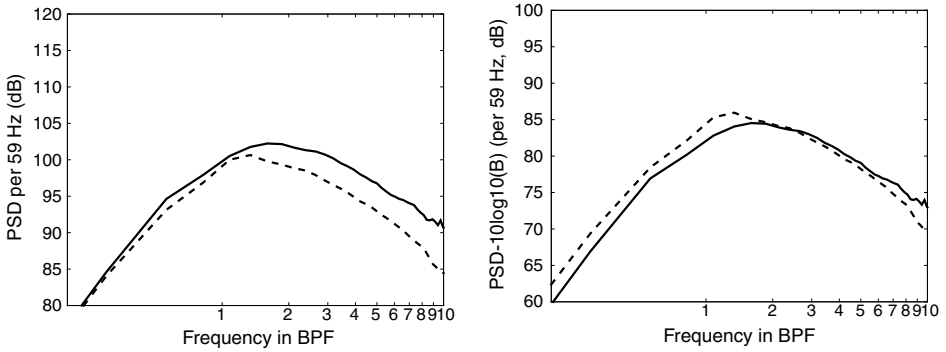

a) Without vane count scaling

b) With vane count scaling $\mu = 1$

Fig. 23 Predicted vane count scaling with chord maintained. NASA SDT approach condition; response = 2 − D equivalence + LINSUB: $B = 54$ **(solid line), and** $B = 26$ **(dotted line).**

The vane count trend of the sound power results from the combined effects of

$$\sum \Phi_{ww}/S$$

and $\hat{h}_{mn}^{\pm}$ [Eq. (16)]. It depends on many factors: mainly, the vane count and the frequency. If C is maintained,

$$\sum \Phi_{ww}/S$$

and $\hat{h}_s^+$ are independent of B for $B < B_c$; sound power scales with B, and therefore $\mu = 1$. For $B \gg B_c$,

$$\sum \Phi_{ww}/S$$

and $\hat{h}_s^+$ scale with B and $1/B$, respectively; sound power is independent of B and $\mu = 0$. Since B_c increases with frequency, $\mu = 0 \rightarrow 1$ is expected in the PSD spectra as the frequency increases.

Figure 23a depicts the predicted PSDs at the SDT approach condition for two vane counts (54 and 26) with the chord fixed. The noise levels for $B = 26$ and for $B = 54$ are almost the same at low frequency, suggesting $\mu = 0$. In the high-frequency range, the two curves with $\mu = 1$ scaling in Fig. 23b collapse well. This is consistent with the aforementioned analyses.

A similar analysis can be made when solidity is maintained. In the low-frequency range, μ is −1 for small B (less than four), and zero for larger B (greater than 11). At high frequency, $\mu = 0$ for regular B (less

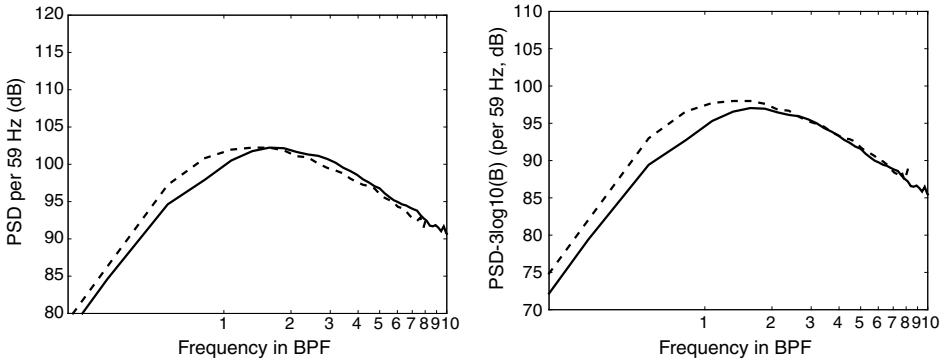

a) Without vane count scaling

b) With vane count scaling $\mu = 0.3$

Fig. 24 Predicted vane count scaling with solidity maintained. NASA SDT approach condition; response = 2-D equivalence + LINSUB: $B = 54$ **(solid line), and** $B = 26$ **(dotted line).**

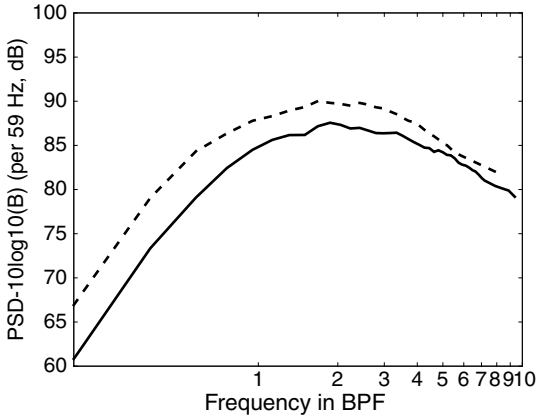

Fig. 25 Predicted vane count scaling $\mu = 1$ at cutback, with constant solidity; response = 2-D equivalence + LINSUB: $B = 54$ (solid line), and $B = 26$ (dotted line).

than 65), and $\mu = 1$ for very large B (greater than 128). Reducing the vane count is noise beneficial only in the very high-frequency range. The predictions in Fig. 24a are consistent with this analysis: the noise level for the low vane count is higher at low frequency, and it is only slightly lower at high frequency ($\mu \sim 0$). Also, $\mu = 0.3$ instead of $\mu = 1$ best fits in the high-frequency range, as shown in Fig. 24b. It is believed that, at the approach condition, the whole spectrum is still in the midfrequency range. When frequency goes even higher, $\mu = 1$ applies, such as a greater than 5 BPF at the cutback condition, shown in Fig. 25.

The current method has mixed success in predicting vane count trends in the SDT. The noise increase ($\mu < 0$) in the low-frequency range and $\mu = 1$ at very high frequency are predicted. However, $\mu = 1$ scaling applies at a frequency as low as 2.5 BPF in the test (Fig. 14). This implies that the current model overpredicts the trailing-edge effect by ignoring the camber. Predictions using the single-airfoil high-frequency approximation, shown in Fig. 26, give $\mu = 1$ scaling. This is consistent with the analysis of the single-airfoil response, shown in Fig. 22.

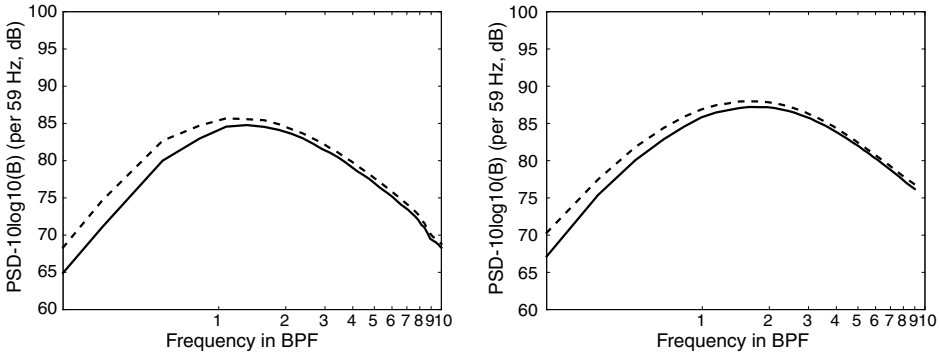

a) Approach **b) Takeoff**

Fig. 26 Predicted vane count scaling $\mu = 1$ using the single-airfoil high-frequency approximation, with constant solidity: $B = 54$ (solid line), and $B = 26$ (dotted line).

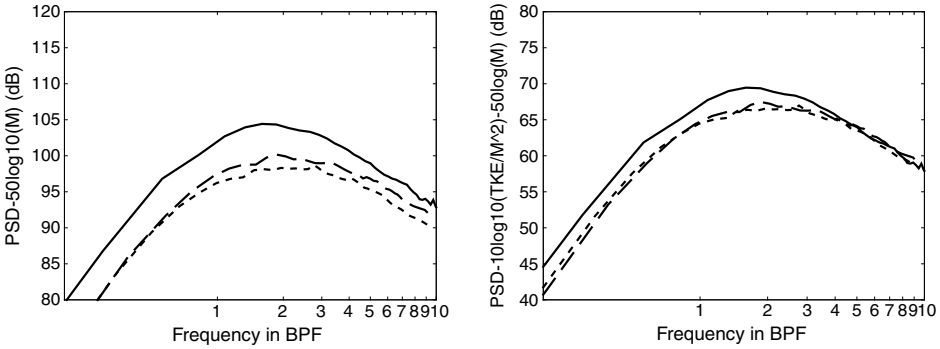

a) M^5 scaling with actual wakes **b) M^5 scaling with 'ideal' wakes**

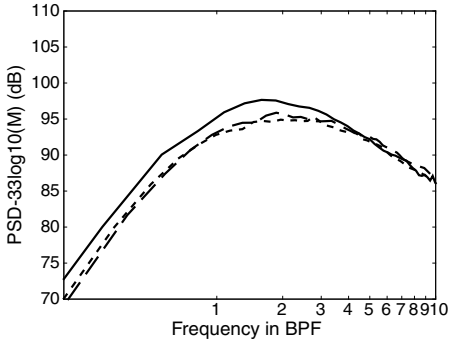

c) $M^{3.3}$ scaling with actual wakes

Fig. 27 Predicted fan speed scaling, with $B = 54$; response = 2-D equivalence + LINSUB: approach (solid line), cutback (dashed line), and takeoff (dotted line).

D. Fan Tip Speed Trend

The response function $R(\xi, k_1, k_2, k_3)$ defined in Eq. (A3) scales with $\lambda^{-1/2}$ or $\sqrt{M}$ for a single airfoil (equations 16 and 17 in [35]). Assume similar scaling for the cascade response. Then, p scales with $u_0\hat{w}R \sim M^{5/2}$ and the sound power scales with $p^2 \sim M^5$ if $\hat{w}$ ideally scales with M. Examining Eqs. (B13) and (7), one may find $\hat{h}^{\pm}_{mn} \sim M^{0.5+}$ and $\langle \hat{W}^{\pm}_{mn} \rangle \sim M^{4+}$ (0.5+ denotes a value higher than 0.5 and smaller than 0.6). The predictions at different operating conditions (fan speeds) for the $B = 54$ configuration in the SDT are compared in Fig. 27. The spectra with M^5 scaling in Fig. 27a do not collapse. Relative to the scaled sound power at takeoff, the PSD is 1.3 dB higher at cutback and 3.2 dB higher at approach. This mismatch is due to the fact that the turbulence intensity (TI) does not exactly scale with M. The takeoff operation point has the highest aerodynamic efficiency, since it is closer to the design point. Relative to the takeoff, the TI is 1 dB higher at cutback and 3.3 dB higher at approach in the mean flow simulations, which is consistent with the discrepancies shown in Fig. 27a. M^5 scaling is confirmed in Fig. 27b, in which the TI is corrected and proportional to M. "Ideal turbulence" is only possible when aerodynamic performance is optimized for each operating point. It is not the case in the SDT. The actual speed scaling depends on the actual geometries and operation conditions. $M^{3.3}$ scaling best fits both the predictions shown in Fig. 27c and the test data shown in Fig. 15. The current model predicts this trend accurately.

VII. Conclusions

A 2-D equivalence method was recently developed for calculating oblique gust/cascade response. To employ LINearized SUBsonic unsteady flow in cascade in this method, a single-airfoil high-frequency approximation was incorporated to eliminate its erroneous response. The effect of fan-wake turbulence modeling on predicting fan/outlet guide vane interaction broadband noise was then investigated. It was found unnecessary to model the circumferential distribution of the turbulence kinetic energy for typical turbofan engines if a uniform turbulence length scale was used.

A quasi-3-D broadband model was developed. Unsteady lift due to an oblique gust was calculated using the 2-D equivalence method. It was coupled with annular duct modes to compute the in-duct total sound power. A larger spanwise integration range was required in the model to ensure integration convergence. A spanwise turbulence integral length for determining this range was given. The proposed model was validated against the NASA SDT data. Sound power scaling with vane count was examined. If the airfoil chord was fixed as the vane count B was reduced, the cascade response approached the single-airfoil response. At low frequency, the sound power was independent of B; it scaled with B at high frequency. If the solidity was kept fixed, the cascade response did not converge on the single-airfoil response, even for very small B. Linear scaling with B only applied at very high frequency. As to sound power scaling with fan speed, two scaling factors were identified: M_T^5 for an ideal wake, in which turbulence intensity scaled with M_T; and $M_T^{3.3}$ for the tested/simulated fan wake, in which turbulence flows were at offdesign conditions at approach and at cutback.

Geometries and mean flows were greatly simplified in the prediction process. The current results demonstrate the value of this reduced-order approach. This confirms the belief that the effects of blade thickness, camber, and angle of attack are mainly on the steady force. Their impacts on unsteady lift and noise are in higher orders.

Appendix A: Two-Dimensional Equivalence Method for Oblique Gust/Cascade Response

Details of the quasi-3-D broadband model are given in the Appendices. The model is also reduced to a 2-D model to compare with an existing theory.

A 2-D equivalence method to compute the oblique gust/cascade response is briefly described here. The detail was presented in [30]. Blades are assumed flat and unloaded. Two Cartesian coordinate systems, (ξ, η, z) and (x, y, z), are established on the reference blade, shown in Fig. 1. The wave number vectors in the two systems are (k_1, k_2, k_3) and (α, β, k_3), respectively. Note the following relations:

$$\xi = x\cos\theta + y\sin\theta, \quad \eta = -x\sin\theta + y\cos\theta,$$
$$\alpha = k_1\cos\theta - k_2\sin\theta, \quad \beta = k_1\sin\theta + k_2\cos\theta, \quad \alpha x + \beta y = k_1\xi + k_2\eta \tag{A1}$$

Unsteady lift from 2-D gust ($k_3 = 0$)/cascade interaction is calculated using LINSUB. For $k_3 \neq 0$, we define a 2-D equivalence problem for cut-on modes [$k_3 \leq \omega/(a_0\gamma)$]. The five input parameters to LINSUB in the 2-D equivalence method are as follows:

Mach number:

$$\bar{M} = M\sqrt{1 - (\gamma k_3 a_0/\omega)^2}, \qquad M = u_0/a_0, \qquad \gamma = \sqrt{1 - M^2}$$

Stagger angle:

$$\bar{\theta} = \tan^{-1}[(\tan\theta)\bar{\gamma}/\gamma], \qquad \bar{\gamma} = \sqrt{1 - \bar{M}^2}$$

Spacing-to-chord ratio:

$$\bar{S}/\bar{C} = (S/C)\sqrt{\sin^2\theta + \cos^2\theta(\gamma/\bar{\gamma})^2} \tag{A2}$$

Reduced frequency:

$$\bar{\lambda} = (\bar{\gamma}/\gamma)^2\lambda, \qquad \lambda = \omega C/u_0$$

and IBPA:

$$\bar{\beta}_s\bar{S} = \beta_s S + \lambda S\,\sin\theta[(\bar{\gamma}/\gamma)^2 - 1]$$

The output of LINSUB is $l^*(\xi, k_1, k_2, k_3)$, which is the unsteady lift distribution on the reference plate normalized by $\bar{\rho}_0\bar{u}_0^2$ for gust strength $\hat{w} = \bar{u}_0$ and time factor $e^{i\bar{\omega}t}$ (where * denotes conjugate). For the oblique gust in Eq. (1), unsteady lift in the time domain on the reference plate is

$$L^0(\xi, z, t, k_1, k_2, k_3) = \rho_0 u_0 \hat{w}(k_1, k_2, k_3) R(\xi, k_1, k_2, k_3) e^{i(k_3 z - \omega t)},$$
$$R(\xi, k_1, k_2, k_3) = (\bar{\gamma}/\gamma) l(\xi, k_1, k_2, k_3) e^{i(1-\bar{\gamma}^2/\gamma^2)\xi\omega/u_0} \tag{A3}$$

The LINSUB/Amiet combination method introduced in Sec. III may also be used in this 2-D equivalence method. However, since $\bar{M} \to 0$ as k_3 increases, $\bar{M}\bar{\lambda}/(1 - \bar{M}^2) > \pi/2$, which is required for high-frequency approximation, may no longer be valid even at high frequency.

Appendix B: Sound Pressure Generated by Unsteady Lift in Annular Duct

A cylindrical coordinate system (x, φ, r) is established in the duct. Uniform mean flow with velocity u_d in the axial x direction is assumed; the analysis is therefore applicable only for exhaust radiated noise. Note the mismatch of this mean flow and the swirling flow u_0 modeled in LINSUB. Some cut-on modes in the axial mean flow are cut off in the swirling flow. These modes are treated as cut off in the current model.

The form of sound pressure Fourier component assumed is

$$p(\boldsymbol{x}, t) = \text{Real}[\hat{p}(\boldsymbol{x}, \omega)e^{-i\omega t}\,\mathrm{d}\omega] \tag{B1}$$

where $\hat{p}(\boldsymbol{x},\omega)$ is the sound pressure spectral density. In a straight, infinitely long hard-walled annular duct,

$$\hat{p}^{\pm}(\boldsymbol{x}_o)=\sum_{m=-\infty}^{\infty}\sum_{n=0}^{\infty}\hat{p}^{\pm}_{mn},\quad \text{where } \hat{p}^{\pm}_{mn}=A^{\pm}_{mn}\Psi_m(\mu_{mn}r_o)e^{i(\alpha^{\pm}_{mn}x_o+m\varphi_o)}$$

$$A^{\pm}_{mn}=\frac{1}{4\pi\Gamma_{mn}\kappa_{mn}}\iint_S\Psi^*_m(\mu_{mn}r)e^{-i(\alpha^{\pm}_{mn}x+m\varphi)}$$

$$\times\left[\alpha^{\pm}_{mn}\hat{f}_x(\boldsymbol{x})+\frac{m}{r}\hat{f}_\varphi(\boldsymbol{x})\right]\mathrm{d}S(\boldsymbol{x})\ \text{and}$$

$$\alpha^{\pm}_{mn}=\frac{-M_dk_d\pm\kappa_{mn}}{1-M_d^2},\quad \kappa_{mn}=\sqrt{k_d^2-(1-M_d^2)\mu^2_{mn}},$$

$$k_d=\omega/a_d,\quad M_d=u_d/a_d \tag{B2}$$

where a_d is the sound speed. The source point is $\boldsymbol{x}$. The observation point $\boldsymbol{x}_o$ is outside of the source region (either upstream or downstream). Also, α^+_{mn} is used for $x_o\geq x$ (downstream) and α^-_{mn} for $x_o<x$ (upstream). Unsteady lift on the fluid is assumed to have components only in the axial and the circumferential directions: $\hat{f}_x$ and $\hat{f}_\varphi$. $\beta=m/r$ is the tangential acoustic wave number. If we define the two-dimensional modal vector $\alpha=(\alpha_{mn},m/r)$, then the modal amplitude $A^{\pm}_{mn}$ is proportional to the unsteady lift projected onto the modal vector: $\boldsymbol{\alpha}\cdot\hat{f}=\alpha^{\pm}_{mn}\hat{f}_x+(m/r)\hat{f}_\varphi$. The eigenvalue is μ_{mn}. The eigenfunction $\Psi_m(\mu_{mn}r)$ in an annular duct is

$$\Psi_m(\mu_{mn}r)=J_m(\mu_{mn}r)-\frac{J'_m(\mu_{mn}R_i)}{Y'_m(\mu_{mn}R_i)}Y_m(\mu_{mn}r) \tag{B3}$$

and

$$\Gamma_{mn}=\int_{R_i}^{R_o}|\Psi_m(\mu_{mn}r)|^2rdr$$

$$=\begin{cases}\frac{1}{2}(R_o^2-R_i^2), m=n=0;\\ \frac{1}{2}(R_o^2-\frac{m^2}{\mu^2_{mn}})\Psi^2_m(\mu_{mn}R_o)-\frac{1}{2}(R_i^2-\frac{m^2}{\mu^2_{mn}})\Psi^2_m(\mu_{mn}R_i),\quad \text{otherwis}\end{cases}$$

R_i and R_o are, respectively, the inner and outer duct radii. $J_m(\mu_{mn}r)$ and $Y_m(\mu_{mn}r)$ are, respectively, the first and the second kinds of Bessel functions of integer order m.

Assume the blades are thin and the fluid is inviscid. The lift exerted by the fluid on the jth blade,

$$\hat{L}^j(\xi,r)\equiv\hat{p}^j_p(\xi,r)-\hat{p}^j_s(\xi,r)=-|\hat{\boldsymbol{f}}(\xi,r)| \tag{B4}$$

where $j=0,1,\ldots,B-1$, is in the direction normal to the blade suction side. The blade normal is $\boldsymbol{n}=(-\sin\theta,\cos\theta)$. The suction-side and pressure-side sound pressure are $\hat{p}^j_s$ and $\hat{p}^j_p$, respectively. Substituting Eq. (B4) into Eq. (B2), the mode amplitude becomes

$$A^{\pm}_{mn}=\frac{1}{4\pi\Gamma_{mn}\kappa_{mn}}\int_{R_i}^{R_o}\Psi^*_m(\mu_{mn}r)(\alpha^{\pm}_{mn}\sin\theta-\frac{m}{r}\cos\theta)$$

$$\times\int_C e^{-i\xi(\alpha^{\pm}_{mn}\cos\theta+m\sin\theta/r)}\sum_{j=0}^{B-1}\hat{L}^j(\xi,r)e^{-im2\pi j/B}\,\mathrm{d}\xi\,\mathrm{d}r \tag{B5}$$

To compute the chordwise distribution of unsteady lift $\hat{L}^j(\xi,r)$ at r, two approximations are to be made. First, variations of the mean flow and the cascade geometry are small within a few radial correlation lengths of unsteady lift. The second is to unwrap the annular cascade to form a linear cascade so that all terms associated with coordinate curvature in the Euler equations can be neglected. With these approximations, the linear Euler equations with uniform flow in the Cartesian coordinates apply. Then, we may employ the equivalent 2-D method introduced in Appendix A to compute unsteady lift $\hat{L}^0(\xi,r)$ on the reference blade.

Wake turbulence is fan locked and has a frozen pattern. In the frame ($\xi'=\xi-u_0t$, η, z) moving with the mean flow, the upwash velocity from a frozen gust is

$$\hat{w}(k_1,k_2,k_3)e^{i(k_1\xi'+k_2\eta+k_3z)}\,\mathrm{d}k_1\,\mathrm{d}k_2\,\mathrm{d}k_3$$

where $\hat{w}(k_1,k_2,k_3)$ is the upwash velocity spectral density. The gust in the fixed frame is

$$\hat{w}(k_1,k_2,k_3)e^{i(k_1\xi+k_2\eta+k_3z-\omega t)}\,\mathrm{d}k_1\,\mathrm{d}k_2\,\mathrm{d}k_3,\qquad \text{where } \omega=k_1u_0 \tag{B6}$$

The nondimensional lift on the reference blade $R(\xi,k_1,k_2,k_3)$ is obtained in Eq. (A3). The unsteady lift in time domain is

$$L^0(\xi,z,t,k_1,k_2,k_3|r)$$
$$=\rho_0(|r)u_0(|r)\hat{w}(k_1,k_2,k_3)\times R(\xi,k_1,k_2,k_3)e^{i(k_3z-k_1u_0t)}\,\mathrm{d}k_1\,\mathrm{d}k_2\,\mathrm{d}k_3$$

where r in $(..|r)$ denotes a parameter and not an independent variable. Note the different Fourier transform used in LINSUB:

$$e^{i(k_1\xi+k_2\eta+k_3z+\omega^*t)}$$

Care must be taken regarding the input parameters to LINSUB and how to relate $l^*(\xi,k_1,k_2,k_3)$ from LINSUB to $R(\xi,k_1,k_2,k_3)$ in the current model.

The IBPA of the gust is

$$\sigma=\beta_vS \tag{B7}$$

where β_v is the tangential vortical wave number. The unsteady lift on each blade is

$$L^j(\xi,z,t)$$
$$=\rho_0u_0\int_{-\infty}^{\infty}\int_{-\infty}^{\infty}\int_{-\infty}^{\infty}\hat{w}(k_1,k_2,k_3)\times R(\xi,k_1,k_2,k_3)e^{ij\sigma}e^{i(k_3z-k_1u_0t)}\mathrm{d}k_1\mathrm{d}k_2\mathrm{d}k_3,$$
$$j=0,1,\ldots,B-1 \tag{B8}$$

The turbulence and unsteady lift are aperiodic stationary random processes. The Fourier transform of the unsteady lift is defined as ([48] appendix A)

$$\hat{L}^j_T(\xi,z)=\frac{1}{2\pi}\int_{-T}^{T}L^j(\xi,z,t)e^{i\omega t}\,\mathrm{d}t \tag{B9}$$

Using

$$\lim_{T\to\infty}\frac{1}{2\pi}\int_{-T}^{T}e^{-i\omega t}\,\mathrm{d}t=\delta(\omega) \tag{B10}$$

in Eqs. (B8) and (B9) yields

$$\lim_{T\to\infty}\hat{L}^j_T(\xi,z)=\rho_0\int_{-\infty}^{\infty}\int_{-\infty}^{\infty}\hat{w}(K_1,k_2,k_3)$$
$$R(\xi,K_1,k_2,k_3)e^{ij\sigma}e^{ik_3z}\,\mathrm{d}k_2\,\mathrm{d}k_3,\qquad K_1=\omega/u_0 \tag{B11}$$

Substitute it into Eq. (B5):

$$A_{mn}^{\pm}=\frac{1}{4\pi\Gamma_{mn}\kappa_{mn}}\int_{R_i}^{R_o}\rho_0\Psi_m^*(\mu_{mn}r)\int_{-\infty}^{\infty}\int_{-\infty}^{\infty}\hat{w}(K_1,k_2,k_3|r)\times\hat{h}_{mn}^{\pm}(K_1,k_2,k_3|r)$$
$$e^{ik_3r}\sum_{j=0}^{B-1}e^{ij(\sigma-m2\pi/B)}\,\mathrm{d}k_2\,\mathrm{d}k_3\,\mathrm{d}r \tag{B12}$$

The chordwise-integrated response function is

$$\hat{h}_{mn}^{\pm}(k_1,k_2,k_3|r)=\left(\alpha_{mn}^{\pm}\sin\theta-\frac{m}{r}\cos\theta\right)$$
$$\times\int_C e^{-i\xi(\alpha_{mn}^{\pm}\cos\theta+m\sin\theta/r)}R(\xi,k_1,k_2,k_3|r)\,\mathrm{d}\xi \tag{B13}$$

The integration can be carried out using the trapezoidal rule in [49], Eq. (16).

Appendix C: Broadband Model

Fourier components of sound pressure $\hat{p}_T(\omega)$ and axial acoustic velocity $\hat{u}_T(\omega)$ can be defined in the same way as in Eq. (B9). The sound intensity in the axial direction is

$$\hat{I}_x=\lim_{T\to\infty}\frac{\pi}{T}\mathrm{Real}\left\{\left(1+M_d^2\right)\hat{p}_T(\omega)\hat{u}_T^*(\omega)\right.$$
$$\left.+M_d\left[\hat{p}_T(\omega)\hat{p}_T^*(\omega)/(\rho_d a_d)+\rho_d a_d\hat{u}_T(\omega)\hat{u}_T^*(\omega)\right]\right\} \tag{C1}$$

The sound power spectrum density in the duct is the sum of the sound power from all cut-on modes:

$$\hat{W}=\int_{R_i}^{R_o}\int_0^{2\pi}\hat{I}_x r\,\mathrm{d}\varphi\,\mathrm{d}r=\sum_m\sum_n\hat{W}_{mn},$$
$$\hat{W}_{mn}^{\pm}=\pm\lim_{T\to\infty}\frac{\pi}{T}\frac{2\pi\Gamma_{mn}}{\rho_d a_d}A_{mn}^{\pm}A_{mn}^{\pm*}\frac{\kappa_{mn}k_d(1-M_d^2)^2}{(k_d\mp M_d\kappa_{mn})^2} \tag{C2}$$

$\hat{W}_{mn}$ does not depend on the modal phase and the axial location. It depends on the axial wave number, frequency, Mach number, and modal amplitude. It is the two-sided PSD per circular frequency. The one-sided PSD per hertz is $4\pi\hat{W}_{mn}$, with a unit of

$$\text{power}\times\text{time}\sim\text{density}\times\text{velocity}^2\times\text{length}^3$$

The temporal cross-power spectral density

$$\lim_{T\to\infty}\frac{\pi}{T}\langle A_{mn}^{\pm}A_{mn}^{\pm*}\rangle$$

is needed to obtain the ensemble average of the sound power

$$\langle\hat{W}_{mn}^{\pm}\rangle$$

From Eq. (B12), we have

$$\langle A_{mn}^{\pm}A_{mn}^{\pm*}\rangle=\frac{1}{(4\pi\Gamma_{mn}\kappa_{mn})^2}\int_{R_i}^{R_o}\int_{R_i}^{R_o}\int_{-\infty}^{\infty}\int_{-\infty}^{\infty}\int_{-\infty}^{\infty}\int_{-\infty}^{\infty}\rho_0(|r)\rho_0(|r')$$
$$\times\Psi_m^*(\mu_{mn}r)\Psi_m(\mu_{mn}r')\hat{h}_{mn}^{\pm}(K_1,k_2,k_3|r)\hat{h}_{mn}^{\pm*}(K_1,k_2',k_3'|r')$$
$$\cdot\sum_{j=0}^{B-1}e^{ij(\sigma-m2\pi/B)}\sum_{j'=0}^{B-1}e^{-ij'(\sigma'-m2\pi/B)}\langle\hat{w}(K_1,k_2,k_3|r)$$
$$\times\hat{w}^*(K_1,k_2',k_3'|r')\rangle e^{i(k_3r-k_3'r')}\,\mathrm{d}k_2'\,\mathrm{d}k_3'\,\mathrm{d}k_2\,\mathrm{d}k_3\,\mathrm{d}r'\,\mathrm{d}r \tag{C3}$$

For a homogeneous, isotropic turbulence flow, the spatial cross-power spectral density of the upwash velocity is

$$\langle\hat{w}(K_1,k_2,k_3)\hat{w}^*(K_1,k_2',k_3')\rangle$$
$$=\langle\hat{w}\hat{w}^*(K_1,k_2,k_3)\rangle\delta(k_2-k_2')\delta(k_3-k_3')$$

Turbulence is not periodic in space. Its spatial cross-power spectral density is defined as

$$\Phi_{ww}(k_1,k_2,k_3)=\lim_{R\to\infty}\frac{\pi}{R}\langle\hat{w}\hat{w}^*(k_1,k_2,k_3)\rangle,\qquad R=Tu_0$$

Then,

$$\lim_{T\to\infty}\frac{\pi}{T}\left\langle\hat{w}\hat{w}^*(k_1,k_2,k_3)\right\rangle=\lim_{T\to\infty}\frac{R}{T}\Phi_{ww}(k_1,k_2,k_3)=u_0\Phi_{ww}(k_1,k_2,k_3)$$

Substitute it into Eq. (C3):

$$\lim_{T\to\infty}\frac{\pi}{T}\langle A_{mn}^{\pm}A_{mn}^{\pm*}\rangle=\frac{1}{(4\pi\Gamma_{mn}\kappa_{mn})^2}\int_{R_i}^{R_o}\int_{R_i}^{R_o}\int_{-\infty}^{\infty}\int_{-\infty}^{\infty}u_0(|r)\rho_0(|r)\rho_0(|r')$$
$$\times\Psi_m^*(\mu_{mn}r)\Psi_m(\mu_{mn}r')\hat{h}_{mn}^{\pm}(K_1,k_2,k_3|r)\hat{h}_{mn}^{\pm*}(K_1,k_2,k_3|r')$$
$$\times\sum_{j=0}^{B-1}e^{ij(\sigma-m2\pi/B)}\sum_{j'=0}^{B-1}e^{-ij'(\sigma-m2\pi/B)}$$
$$\times\Phi_{ww}(K_1,k_2,k_3)e^{ik_3(r-r')}\,\mathrm{d}k_2\,\mathrm{d}k_3\,\mathrm{d}r'\,\mathrm{d}r \tag{C4}$$

where r' must be near r if the mean flow and turbulence are not uniform. This requires a small spanwise integral length of unsteady lift.

Vorticity waves are periodic with fundamental period BS in the tangential direction of the unwrapped duct. Therefore,

$$\sigma/S=\beta_v=K_1\sin\theta+k_2\cos\theta=2\pi l_v/(BS),\quad l_v=0,\pm1,\pm2,\ldots;$$
$$k_2=\frac{2\pi}{BS\cos\theta}l_v-K_1\tan\theta,\quad \mathrm{d}k_2=\frac{2\pi}{BS\cos\theta}\Delta l_v \tag{C5}$$

Note that

$$\sum_{j=0}^{B-1}e^{2\pi ij(l_v-m)/B}=\begin{cases}B, & \text{if } (l_v-m)/B \text{ is an integer,}\\ 0, & \text{otherwise}\end{cases}$$

which leads to the scattering rule:

$$l_v-m=Bj,\qquad j=0,\pm1,\pm2,\ldots$$

Then, the integration over k_2 in Eq. (C4) can be replaced by the summation over the vorticity wave index l_v:

$$\lim_{T\to\infty}\frac{\pi}{T}\langle A^{\pm}_{mn}A^{\pm *}_{mn}\rangle = \frac{B}{8\pi(\Gamma_{mn}\kappa_{mn})^2}\int_{R_i}^{R_o}\int_{R_i-r}^{R_o-r}\frac{u_0(|r)\rho_0(|r)\rho_0(|r+\Delta r)}{S\cos\theta}$$
$$\times\Psi^*_m(\mu_{mn}r)\Psi_m(\mu_{mn}(r+\Delta r))$$
$$\cdot\sum_{j=-\infty}^{\infty}\int_{-\infty}^{\infty}\hat{h}^{\pm}_{mn}\left(K_1,\frac{2\pi(m+Bj)}{BS\cos\theta}-K_1\tan\theta,k_3|r\right)$$
$$\times\hat{h}^{\pm *}_{mn}\left(K_1,\frac{2\pi(m+Bj)}{BS\cos\theta}-K_1\tan\theta,k_3|r+\Delta r\right)$$
$$\cdot\Phi_{ww}\left(K_1,\frac{2\pi(m+Bj)}{BS\cos\theta}-K_1\tan\theta,k_3\right)e^{-ik_3\Delta r}\,\mathrm{d}k_3\,\mathrm{d}\Delta r\,\mathrm{d}r \tag{C6}$$

The unsteady lift is the same for $\sigma = 2\pi(m+Bj)/B$ and $\sigma - 2\pi = 2\pi[m+B(j-1)]/B$:

$$\hat{h}^{\pm}_{mn}\left(K_1,\frac{2\pi(m+jB)}{BS\cos\theta}-K_1\tan\theta,k_3\right) = \hat{h}^{\pm}_{mn}\left(K_1,\frac{2\pi m}{BS\cos\theta}-K_1\tan\theta,k_3\right) \tag{C7}$$

Substitute Eqs. (C6) and (C7) into Eq. (C2):

$$\langle\hat{W}^{\pm}_{mn}\rangle = \pm\frac{B}{4\rho_d a_d\Gamma_{mn}\kappa_{mn}}\frac{k_d(1-M_d^2)^2}{(k_d\mp M_d\kappa_{mn})^2}$$
$$\times\mathrm{Real}\left\{\int_{R_i}^{R_o}\int_{R_i-r}^{R_o-r}\frac{u_0(|r)\rho_0(|r)\rho_0(|r+\Delta r)}{S\cos\theta}\Psi^*_m(\mu_{mn}r)\Psi_m(\mu_{mn}(r+\Delta r))\right.$$
$$\cdot\int_{-\infty}^{\infty}\hat{h}^{\pm}_{mn}\left(K_1,\frac{2\pi m}{BS\cos\theta}-K_1\tan\theta,k_3|r\right)$$
$$\times\hat{h}^{\pm *}_{mn}(K_1,\frac{2\pi m}{BS\cos\theta}-K_1\tan\theta,k_3|r+\Delta r)$$
$$\left.\cdot\left[\sum_{j=-\infty}^{\infty}\Phi_{ww}\left(K_1,\frac{2\pi(m+Bj)}{BS\cos\theta}-K_1\tan\theta,k_3\right)\right]e^{-ik_3\Delta r}\mathrm{d}k_3\,\mathrm{d}\Delta r\mathrm{d}r\right\} \tag{C8}$$

Note the singularity when $\kappa_{mn} = 0$ at the cut-on frequency.

Appendix D: Sound Power Spectrum in Two Dimensions

The quasi-3-D model [Eq. (C8)] is reduced to two dimensions to compare with the theory in [23]. Assume the annular duct width $b(= R_o - R_i)$ is much smaller than the mean radius $R_c[= (R_o + R_i)/2]$, i.e., $b/R_c \to 0$ and $R_i/R_o \to 1$. There is a plane wave for each spinning mode m: $n = 0, \mu_{m0} = 0, \Psi_m(\mu_{m0}r) = 1$, $\Gamma_{m0} = (R_o^2 - R_i^2)/2 = bR_c$, and $\kappa_{mn} = k_d$. Assume the flow is inviscid or b is much larger than the boundary-layer thicknesses. The mean flow, the turbulence statistics, and the gust/cascade response do not vary over Δr:

$$\hat{h}^{\pm}_{mn}(k_1,k_2,k_3|r) \approx \hat{h}^{\pm}_{mn}(k_1,k_2,k_3|r+\Delta r)$$

Then, Eq. (C6) becomes

$$\lim_{T\to\infty}\frac{\pi}{T}\langle A^{\pm}_{m0}A^{\pm *}_{m0}\rangle = \frac{B}{8\pi(\Gamma_{m0}\kappa_{m0})^2}\frac{u_0\rho_0^2}{S\cos\theta}$$
$$\times\int_{R_i}^{R_o}\int_{-\infty}^{\infty}\left|\hat{h}^{\pm}_{m0}\left(K_1,\frac{2\pi m}{BS\cos\theta}-K_1\tan\theta,k_3\right)\right|^2$$
$$\cdot\sum_{j=-\infty}^{\infty}\Phi_{ww}\left(K_1,\frac{2\pi(m+Bj)}{BS\cos\theta}-K_1\tan\theta,k_3\right)\left[\int_{R_i-r}^{R_o-r}e^{-ik_3\Delta r}\mathrm{d}\Delta r\right]\mathrm{d}k_3\,\mathrm{d}r$$

As $b \to 0$,

$$\int_{R_i-r}^{R_o-r}e^{-ik_3\Delta r}\,\mathrm{d}\Delta r = be^{-ik_3(R_c-r)}\,\mathrm{sinc}(k_3b/2) \to be^{-ik_3(R_c-r)},$$
$$\int_{R_i}^{R_o}e^{ik_3r}\,\mathrm{d}r = be^{ik_3R_c}\,\mathrm{sinc}(k_3b/2) \to be^{ik_3R_c}$$

Then,

$$\lim_{T\to\infty}\frac{\pi}{T}\langle A^{\pm}_{m0}A^{\pm *}_{m0}\rangle \to \frac{Bb^2}{8\pi(\Gamma_{m0}\kappa_{m0})^2}\frac{u_0\rho_0^2}{S\cos\theta}$$
$$\times\int_{-\infty}^{\infty}\left|\hat{h}^{\pm}_{m0}\left(K_1,\frac{2\pi m}{BS\cos\theta}-K_1\tan\theta,k_3\right)\right|^2$$
$$\times\sum_{j=-\infty}^{\infty}\Phi_{ww}\left(K_1,\frac{2\pi(m+Bj)}{BS\cos\theta}-K_1\tan\theta,k_3\right)\mathrm{d}k_3$$

Substituting it into Eq. (C2), we obtain the sound power spectrum for a two-dimensional case:

$$\langle\hat{W}^{\pm}_{m0}\rangle \to \pm\frac{\pi b(1-M_d^2)^2}{2(k_d\mp M_dk_d)^2}\frac{M\rho_0}{S^2\cos\theta}$$
$$\times\int_{-\infty}^{\infty}\left|\hat{h}^{\pm}_{m0}\left(K_1,\frac{2\pi m}{BS\cos\theta}-K_1\tan\theta,k_3\right)\right|^2$$
$$\cdot\sum_{j=-\infty}^{\infty}\Phi_{ww}\left(K_1,\frac{2\pi(m+Bj)}{BS\cos\theta}-K_1\tan\theta,k_3\right)\mathrm{d}k_3 \tag{D1}$$

The Sound power spectrum density per span

$$\langle\hat{W}^{\pm}_{m0}\rangle/b$$

is the same as the 2-D result [Eq. (25)] in [23], except that the response

$$R_l(k_1,k_2) = -\hat{h}^{\pm}_{mn}(k_1,k_2,k_3)/(2Sk_d)$$

is assumed same for all k_3 in [23].

Note that span b is not required to be small compared with the turbulence integral length scale in this analysis.

Acknowledgments

The authors would like to thank their colleagues Umesh Paliath, Trevor Wood, Kishore Ramakrishnan, Nikolai Pastouchenko, and Lawrence Cheung (GE Global Research); and Muni Majjigi and John Wojno (GE Aviation) for their fruitful discussions. The authors would also like to acknowledge Gary G. Podboy (NASA John H. Glenn Research Center) for providing the Source Diagnostic Test turbulence test data.

References

[1] Gliebe, P. R., "The GE90: Quiet by Design, Quieter Aircraft Engines Through Leveraging New Technologies," *Presentation for 2003 Berkeley Airport Noise Symposium*, March 2003; also Thomas, R. H., Burley, C. L., and Olson, E. D., "Hybrid Wing Body Aircraft System Noise Assessement with Propulsion Airframe Aeroacoustics Experiments," *Presentation for 2003 Berkeley Airport Noise Symposium*, AIAA Paper 2010-3913, 2010.

[2] Gliebe, P. R., Ho, P. Y., and Mani, R., "UHB Engine Fan Broadband Noise Reduction Study," NASA Lewis Research Center Final Rept. NAS3-26617, Task Order 3, May 1995.

[3] Clair, V., Polacsek, C., Garrec, T. L., and Reboul, G., "CAA Methodology to Simulate Turbulence-Airfoil Noise," AIAA Paper 2012-2189, 2012.

[4] Morin, B. L., "Broadband Fan Noise Prediction System for Turbofan Engines," Setup_BFaNS User's Manual and Developer's Guide, Vol. 1, NASA Rept. CR-2010-216898, Nov. 2010.

[5] Ganz, U. W., Joppa, P. D., Patten, T. J., and Scharpf, D. F., "Boeing 18-Inch Fan Rig Broadband Noise Test," NASA Rept. CR-1998-208704, 1998.

[6] Moreau, A., and Enghardt, L., "Ranking of Fan Broadband Noise Sources Based on an Experimental Parametric Study," AIAA Paper 2009-3222, 2009.

[7] Moreau, S., and Roger, M., "Competing Broadband Noise Mechanisms in Low-Speed Axial Fans," *AIAA Journal*, Vol. 45, No. 1, 2007, pp. 48–57. doi:10.2514/1.14583

[8] Moreau, A., and Oertwig, S., "Measurements Compared to Analytical Prediction of the Sound Emitted by a High-Speed Fan Stage," AIAA Paper 2013-2047, 2013.

[9] Hanson, D. B., "Theory for Broadband Noise of Rotor and Stator Cascades with Inhomogeneous Inflow Turbulence Including Effects of Lean and Sweep," NASA Rept. CR-2001-210762, 2001.

[10] Amiet, R. K., "Acoustic Radiation From an Airfoil in a Turbulent Stream," *Journal of Sound and Vibration*, Vol. 41, No. 4, 1975, pp. 407–420. doi:10.1016/S0022-460X(75)80105-2

[11] Adamczyk, J. J., "Passage of a Swept Airfoil Through an Oblique Gust," *Journal of Aircraft*, Vol. 11, No. 5, 1974, pp. 281–287; also NASA Rept. CR-2395, 1974. doi:10.2514/3.59240

[12] Envia, E., "A High Frequency Model of Cascade Noise," AIAA Paper 1998-2318, 1998.

[13] Glegg, S. A. L., "The Response of a Swept Blade Row to a Three-Dimensional Gust," *Journal of Sound and Vibration*, Vol. 227, No. 1, 1999, pp. 29–64. doi:10.1006/jsvi.1999.2327

[14] Posson, H., Roger, M., and Moreau, S., "On a Uniformly Valid Analytical Rectilinear Cascade Response Function," *Journal of Fluid Mechanics*, Vol. 663, Nov. 2010, pp. 22–52. doi:10.1017/S0022112010003368

[15] Namba, M., "Three-Dimensional Analysis of Blade Force and Sound Generation for an Annular Cascade in Distorted Flows," *Journal of Sound and Vibration*, Vol. 50, No. 4, 1977, pp. 479–508. doi:10.1016/0022-460X(77)90498-9

[16] Ventres, C. S., Theobald, M. A., and Mark, W. D., "Turbofan Noise Generation, Volume 1: Analysis," NASA Rept. CR-167952, 1982.

[17] Smith, S. N., "Discrete Frequency Sound Generation in Axial Flow Turbomachines," British Aeronautical Research Council, RandM 3709, London, 1973.

[18] Posson, H., Moreau, S., and Roger, M., "Fan-OGV Broadband Noise Prediction Using a Cascade Response," AIAA Paper 2009-3150, 2009.

[19] Posson, H., Moreau, S., and Roger, M., "On the Use of a Uniformly Valid Analytical Cascade Response Function for Fan Broadband Noise Predictions," *Journal of Sound and Vibration*, Vol. 329, No. 18, 2010, pp. 3721–3743. doi:10.1016/j.jsv.2010.03.009

[20] Posson, M. S., and Roger, M., "Broadband Noise Prediction of Fan Outlet Guide Vane Using a Cascade Response Function," *Journal of Sound and Vibration*, Vol. 330, No. 25, 2011, pp. 6153–6183. doi:10.1016/j.jsv.2011.07.040

[21] Nallasamy, M., and Envia, E., "Computation of Rotor Wake Turbulence Noise," *Journal of Sound and Vibration*, Vol. 282, No. 5, 2005, pp. 649–678. doi:10.1016/j.jsv.2004.03.062

[22] Grace, S., Wixom, A., Winkler, J., Sondak, D., and Logue, M. M., "Fan Broadband Interaction Noise Modeling," AIAA Paper 2012-2269, 2012.

[23] Cheong, C., Joseph, P., and Lee, S., "High Frequency Formulation for the Acoustic Power Spectrum Due to Cascade-Turbulence Interaction," *Journal of the Acoustical Society of America*, Vol. 119, No. 1, 2006, Paper 108. doi:10.1121/1.2139626

[24] Atassi, H. M., and Logue, M. M., "Modeling Tonal and Broadband Interaction," *Procedia Engineering*, Vol. 6, 2010, pp. 214–223. doi:10.1016/j.proeng.2010.09.023

[25] Greschner, B., and Thiele, F., "Broadband Noise Analysis of a Rotor-Stator-Cascade Using Wall Modeled LES Simulation," AIAA Paper 2012-2308, 2012.

[26] Laborderie, L., Moreau, S., and Berry, A., "Compressor Stage Broadband Noise Prediction Using a Large-Eddy Simulation and Comparisons with a Cascade Response Model," AIAA Paper 2013-2042, 2013.

[27] Reba, R. A., and Morin, B. L., "The Gust Response of an Acoustically Treated Flat-Plate Cascade," AIAA Paper 2008-2898, 2008.

[28] Hughes, C. E., "Aerodynamic Performance of Scale-Model Turbofan Outlet Guide Vanes Designed for Low Noise," AIAA Paper 2002-0374, 2002.

[29] Sharma, A., Chen, H., and Shieh, C. M., "Linearized Navier–Stokes Analysis for Rotor-Stator Interaction Tone Noise Prediction," AIAA Paper 2010-3744, 2010.

[30] Ju, H., and Mani, R., "A Semi-Analytical Method for Oblique Gust-Cascade Interaction" (to be submitted).

[31] Cheong, C., Jurdic, V., and Joseph, P., "Decomposition of Modal Acoustic Power Due to Cascade–Turbulence Interaction," *Journal of Sound and Vibration*, Vol. 324, Nos. 1–2, 2009, pp. 57–73. doi:10.1016/j.jsv.2009.01.059

[32] Runyan, H. L., and Watkins, C. E., "Considerations on the Effect of Wind-Tunnel Walls on Oscillating Air Forces for Two-Dimensional Subsonic Compressible Flow," NACA Rept. 1150, 1953.

[33] Lane, F., and Friedman, M., "Theoretical Investigation of Subsonic Oscillatory Blade-Row Aerodynamics," NACA Rept. TN-4136, 1958.

[34] Jenkins, G., Powles, C. J., Blandeau, V. P., and Joseph, P. F., "Low and High Frequency Models for the Prediction of Noise Due to Cascade-Turbulence Interaction," AIAA Paper 2011-2826, 2011.

[35] Amiet, R. K., "High Frequency Thin-Airfoil Theory for Subsonic Flow," *AIAA Journal*, Vol. 14, No. 8, 1976, pp. 1076–1082. doi:10.2514/3.7187

[36] Blandeau, V. P., Joseph, P. F., Jenkins, G., and Powles, C. J., "Sound Power Due to an Airfoil of Arbitrary Stagger Angle in a Turbulent Flow," AIAA Paper 2011-2828, 2011.

[37] Martinez, R., and Widnall, S. E., "Unified Aerodynamic-Acoustic Theory for a Thin Rectangular Wing Encountering a Gust," *AIAA Journal*, Vol. 18, No. 6, 1980, pp. 636–645. doi:10.2514/3.7675

[38] Jurdic, V., Moreau, A., Joseph, P., Enghardt, L., and Coupland, J., "A Comparison Between Measured and Predicted Fan Broadband Noise Due to Rotor-Stator Interaction," AIAA Paper 2007-3692, 2007.

[39] Soulat, L., Posson, H., and Moreau, S., "Wake Model Effects on the Prediction of Turbulence-Interaction Broadband Noise in a Realistic Compressor Stage," AIAA Paper 2011-3900, 2011.

[40] Dieste, M., and Gabard, G., "Broadband Fan Interaction Noise Using Synthetic Inhomogeneous Non-Stationary Turbulence," AIAA Paper 2011-2708, 2011.

[41] Grace, S. M., Maunus, J., Douglas, L., and Sondak, D. L., "Effect of CFD Wake Prediction in a Hybrid Simulation of Fan Broadband Interaction Noise," AIAA Paper 2011-2875, 2011.

[42] Woodward, R. P., and Hughes, C. E., "Fan Noise Source Diagnostic Test —Far-Field Acoustic Results," AIAA Paper 2002-2427, 2002.

[43] Envia, E., "Fan Noise Source Diagnostic Test—Vane Unsteady Pressure Results," AIAA Paper 2002-2430, 2002.

[44] Hughes, C. E., Jeracki, R. J., Woodward, R. P., and Miller, C. J., "Fan Noise Source Diagnostic Test — Rotor Alone Aerodynamic Performance Results," AIAA Paper 2002-2426, 2002.

[45] Kamruzzaman, M., Lutz, T., Wurz, W., and Kramer, E., "On the Length Scales of Turbulence for Aeroacoustic Applications," AIAA Paper 2011-2734, 2011.

[46] Podboy, G. G., Krupar, M. J., Helland, S. M., and Hughes, C. E., "Steady and Unsteady Flow Field Measurements Within a NASA 22 Inch Fan Model," AIAA Paper 2002-1033, 2002.

[47] Posson, H., and Moreau, S., "Effect of Rotor Shielding on Fan–Outlet Guide Vanes Broadband Noise Prediction," *AIAA Journal*, Vol. 51, No. 7, 2013, pp. 1576–1592. doi:10.2514/1.J051784

[48] Goldstein, M. E., "Aeroacoustics," NASA Rept. SP-346, 1976.

[49] Whitehead, D. S., "Force and Moment Coefficients for Vibrating Aerofoils in Cascade," British Aeronautical Research Council, R&M 3254, 1962.

G. Blaisdell
Associate Editor